ZW1.2 Microstructure and microchemistry of undeformed selected samples

by MaP and GeoStructures

Final report

Client: Nouryon Industrial Chemicals, since 12 January 2021 Nobian

PO: 4501373963

April 10th 2023

by

5.1.2.e

With contributions from: 5.1.2.e

[1]MaP Microstructure and Pores GmbH

[2]**Geo**Structures

Approved/reviewed by

5.1.2.e

[3]smartTectonics

[4]Brouard Consulting

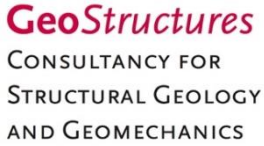

Contents

List of Figures

List of Tables

Summary

In this report, we present a microstructural analysis of samples selected from the available cores of the Zuidwending salt dome with the aim of (i) determining the differential stresses and rheological properties of the evaporite mass during the evolution of the Zuidwending salt dome, and (ii) identifying the material parameters for the constitutive equations, which are relevant for the formation of the present-day "Ist-Zustand", and deformation and permeation during operation and abandonment of solution mined caverns in this salt body.

The observations and theoretical background on which this interpretation is based are discussed in detail in the KEM-17 report and will not be repeated here, so we do not include detailed references in this report and instead refer to KEM-17.

The rock salt studied in this work package belongs to the KRISTALLBROCKENSALZ, which is a well-known salt tectonite in Zechstein II with layering subvertical (i.e., core) in the salt dome. These core-pieces cover all available stratigraphic units and extend over a depth range of 1750 m. The selection of cores in work package ZW1.1 was made with the aim of identifying suitable samples for the deformation and permeation experiments to be carried out in work packages ZW2.2, ZW2.3 and ZW3.2, for which rather homogeneous cores of fine-grained material were required in the majority. Due to this circumstance, the samples selected for this work package and described in this report mainly represent the fine-grained matrix Halite and only occasionally contain Halite mega-grains (Kristallbrocken).

Optical Microscopy (OM) was performed in transmitted and reflected light, on polished and chemically etched thin sections. Some samples were Gamma-irradiated to decorate crystal defects. Broad Ion Beam polishing and Scanning Electron Microscopy (BIB-SEM) was used to image grain boundary damage and in-situ grain boundary structure and Energy Dispersive Spectroscopy (EDS) to characterize the second phase impurity content. The acquired images were analyzed using modern material science methods, and segmented and quantified using image processing methods developed by MaP.

The macro- and microstructural investigations clearly show the three structural elements: (i) mega-grains of Halite, decimeter(s) long and up to 2 cm thick, (ii) fine-grained Halite matrix, and (iii) thin (few mm thick) folded and boudinaged layers of fine-grained Anhydrite. The mega-grains are aligned subparallel to bedding, and the fine-grained Halite matrix forms a variable fraction of the rock. Overall, we observed tight and thus non-permeable grain boundaries with equilibrated, unconnected micropore arrays of fluid inclusions within the Halite fraction of the samples. Some grain boundaries were dilated caused by core damage. The mega-grains were boudinaged and the presence of subgrains indicated internal deformation by dislocation creep. Matrix Halite was deformed by combined dislocation and pressure solution creep, and dynamic recrystallization. The rheology of the Zuidwending salt is interpreted to be that of the mixture of the two components, with the strain rate being strongly dependent on the local presence of the mega-grains.

The average, 2D, median grain size measured in 30 thin section samples is 1.2mm (Std.Dev 2.4mm). The average content of insoluble second phases was 5.0 Vol.% in litho-classF, 5.8 Vol.% in litho-class G and 17.7 Vol.% in litho-class H (litho-classes defined in ZW1.1). Subgrain size piezometry implies that the salt was exposed to a maximum differential stress of 1.8-2.3MPa.

In a paper coauthored by us (Barabasch et al, 2023), which analysed samples from the same formation, strong evidence is presented for large grainsize-dependent differences in Halite rheology based on microstructural observations from rock salt cores from the Zechstein of the Northern Netherlands that experienced different degrees of tectonic deformation. The study compares samples from the relatively undeformed Z2 (Stassfurt) layered salt from Barradeel with much stronger deformed equivalents in diapiric salt from Heiligerlee, Zuidwending, and Pieterburen. Barabasch et al. (2023) use amongst others, the same methods as used for our analysis presented in this report and come to the following conclusions, which are fully confirmed by our analyses performed on the Zuidwending samples:

"*The domal salt samples are typical of the well-known "Kristallbrocken" salt, with cm-thick megacrystals alternating with fine grained Halite and thin Anhydrite layers in Baradeel, and cm-size tectonically disrupted megacrystals surrounded by fine grained Halite with grain size of a few mm in the diapiric salt. Microstructures show much higher strains in fine grained Halite as shown by folding and boudinage of thin Anhydrite layers, as compared to the megacrystals, which are internally much less deformed and develop subgrains during dislocation creep. Subgrain size shows comparable differential stresses in Kristallbrocken than in matrix salt. The fine-grained matrix salt is dynamically recrystallized, has few subgrains and microstructures indicating deformation by solution-precipitation processes.*"

The conclusion of the paper was that the finer grained Halite deformed via dominant pressure solution and the megacrystals by dislocation creep and the research provided strong evidence that "*the fine-grained matrix salt is much weaker than Kristallbrocken because of different dominant deformation mechanisms. This is in agreement with microphysical models showing that grainsize has a dramatic effect on strain rate at these low differential stress, providing evidence for the operation of pressure solution creep in rock salt at differential stress of a few MPa. It shows that including results of microstructural analysis can strongly improve constitutive models of rock salt at low differential stresses relevant in most salt tectonic settings. The authors recommend that this mechanism is included in the constitutive laws describing deformation of engineered structures in rock salt.*" (Barabasch et al., 2023).

Introduction

The aim of this work package is the description and analysis of the sample material selected in ZW1.1, regarding the microstructural properties and rheology and transport properties of the salt with special emphasis on the deformation mechanisms and microporosity recorded in the microstructure. We studied the characteristics that influence the microphysical properties of the salt, such as microcracks, connectivity of grain boundary microporosity, the grain size, the impurity content, and the mineral chemistry.

We describe the present-day microstructural properties (Ist-Zustand) of the pristine salt as determined by state-of-the-art microanalytical imaging technologies in combination with image analysis and (bulk) chemical measurements. We quantified grain size, subgrain size, impurity content, and report on the mineral chemistry and microporosity. Furthermore, an assessment of the deformation mechanisms dislocation creep, grain size-dependent pressure-solution creep, as well as a description of features that influence the salts' rheology and transport properties, such as grain boundary structure, grain boundary fluid distribution, and impurity pinning are part of this report.

Finally, we synthesize our observations and interpretations to provide a recommendation for the constitutive equations and mechanical units to be used in geomechanical modelling of the Ist-Zustand, cavern operation and cavern abandonment. NB: these are reasonable recommendations based on preliminary results, which will be updated after the full results of the different experimental work packages are evaluated.

Methods

We made use of state-of-the-art microanalytical tools to study the microstructure from cm-nm scale comprising Flatbed scanning, Optical Microscopy (OM), Scanning Electron Microscopy (SEM) in combination with Energy Dispersive Spectroscopy (EDS) and Broad Ion Beam (BIB) sputtering. Additional chemical analysis was done using X-Ray Diffraction Analysis (XRD). The bulk content of non- or weak soluble second phases was determined by dissolution of powdered sample material in water. Gamma-irradiation on selected sample slabs was used prior to thin section preparation and optical microscopy to decorate substructures within the Halite crystal lattice. A detailed description of the different analyses and tools is given below (Table 1).

Flatbed scans

High-resolution flatbed scans in transmitted light were used to study the overall microstructure of the thin section samples. Pixel size of these scans was 5.3µm. (Fig. 1, see figure captions for more details).

It is interesting to note that although the flatbed scans (transmitted light is better than reflected light) give some indications of the grainsize of the rock salt, the proper reflected light analysis gives quite significantly different values as the smaller grains are underestimated. For this reason, for example because the method used by Thiemeyer et al., (2016) relies on reflected light mapping in flatbed scans, values in the literature have to be treated with caution.

Optical Microscopy and decoration of microstructures using Gamma irradiation

Grain size and subgrain size measurements, as well as the analysis of second phase impurities and microstructural processes was done using thin sections (e.g., Fig. 1) selected from the slab and core photographs (ZW1.1, Appendix A). The non-irradiated thin sections have a thickness of about 1 mm and are thus transparent in the Halite parts. We used Gamma irradiation on selected sample material, prior to the thin section preparation, for optical investigation and analysis/quantification of crystal lattice features, such as the presence of dislocations and subgrains within the typically transparent and isotropic sample material (Fig. 2). Furthermore, the technology enabled the assessment of the age relationships of the different crystal generations in partly recrystallized samples. The Gamma irradiation was subcontracted to the FRM2 research reactor in Munich. The duration of irradiation was 120 days. The samples were shifted in the irradiation container three times after quarter of the total irradiation time with the aim of achieving a uniform irradiation dose of 1.7 MGy for all samples. It was ensured that a temperature of 75 °C was maintained but not exceeded. From the Gamma irradiated samples, we prepared thin sections and studied them using plane-polarized light in the Optical Microscope (OM) as described in the following paragraph. The thickness of the Gamma-irradiated thin sections was about 100µm.

Optical Microscopy was done using a Zeiss Axioscan 7 microscope equipped with a xy-scanning stage. We used the 2.5x, 5x, and 10x objective producing micrographs with a pixel size of 3.45 µm, 1.38 µm, and 0.6 9µm, respectively. The stitched mosaic micrographs used for grain segmentation were acquired with the 10x objective and were compressed for grain size measurements down to a pixel resolution of 3.45 µm.

Micrographs acquired in reflected light (Fig. 3a) were used to measure grain- and subgrain size within the recrystallized parts of the thin sections (Fig. 3b). For this purpose, the thin section surfaces were etched closely following the protocol proposed by Urai et al. (1987) immersing the polished thin section into

slightly under-saturated NaCl-brine for the duration of 8-13s followed by removal of the brine using n-Hexane or pressurized air. Micrographs acquired in transmitted, plane-polarized light were used to investigate the grain boundary (fluid) morphology, as well as the nature and distribution of second phase impurities such as Anhydrite grains, enclosed into Halite grains and grain boundaries, and microcracks. Micrographs acquired in transmitted, crossed-polarized light were used to identify the nature and distribution of second phase inclusions with anisotropic optical properties (birefringence), such as Anhydrite.

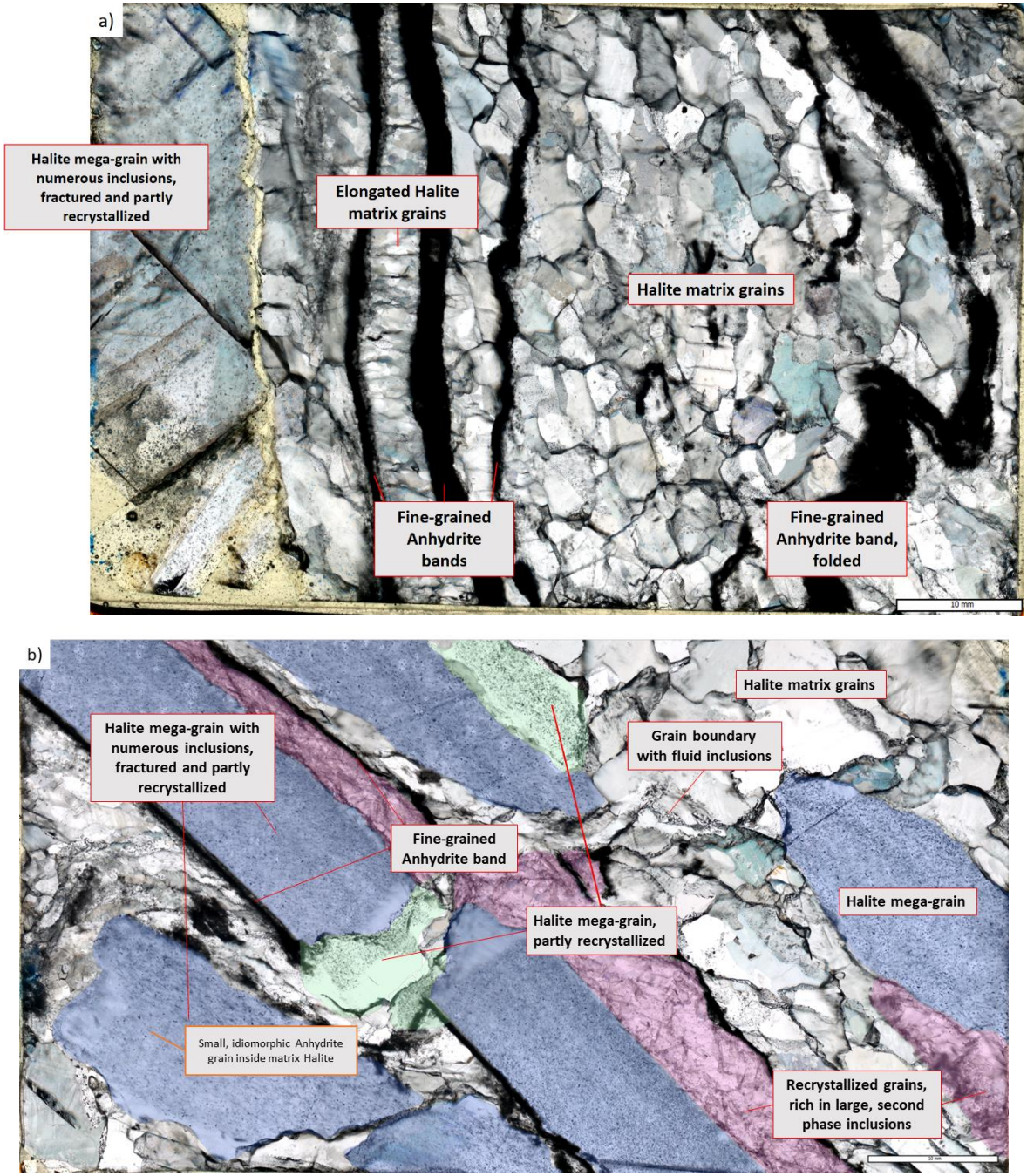

Fig. 1 a) Transmitted light micrograph (flatbed-scan) of Kristallbrockensalz. The inclusion rich mega-grain with subgrains is replaced by strain-induced, fluid-assisted grain boundary migration recrystallization. The surrounding fine-grained Halite deforms by pressure solution and is much weaker during tectonic deformation at low differential stress than the mega-grain, which deform

by dislocation creep. The strongly deformed Anhydrite layers indicating large strain deformation during the evolution of the salt dome. Sample ID ZW_MaP_23 (ZWD-A6A_1_8_605.00m. b) Transmitted light micrograph (flatbed-scan) of typical Kristallbrockensalz. The inclusion/rich mega-grain is replaced by strain-induced, fluid-assisted grain boundary migration recrystallization. Fine-grained Anhydrite bands and recrystallized grains rich in large second phase inclusions border the mega-grains. At the slab-scale the mega-grains show boudinage. Sample ID: ZW_MaP_31 (ZWD-A8A_4_8_1090.63).

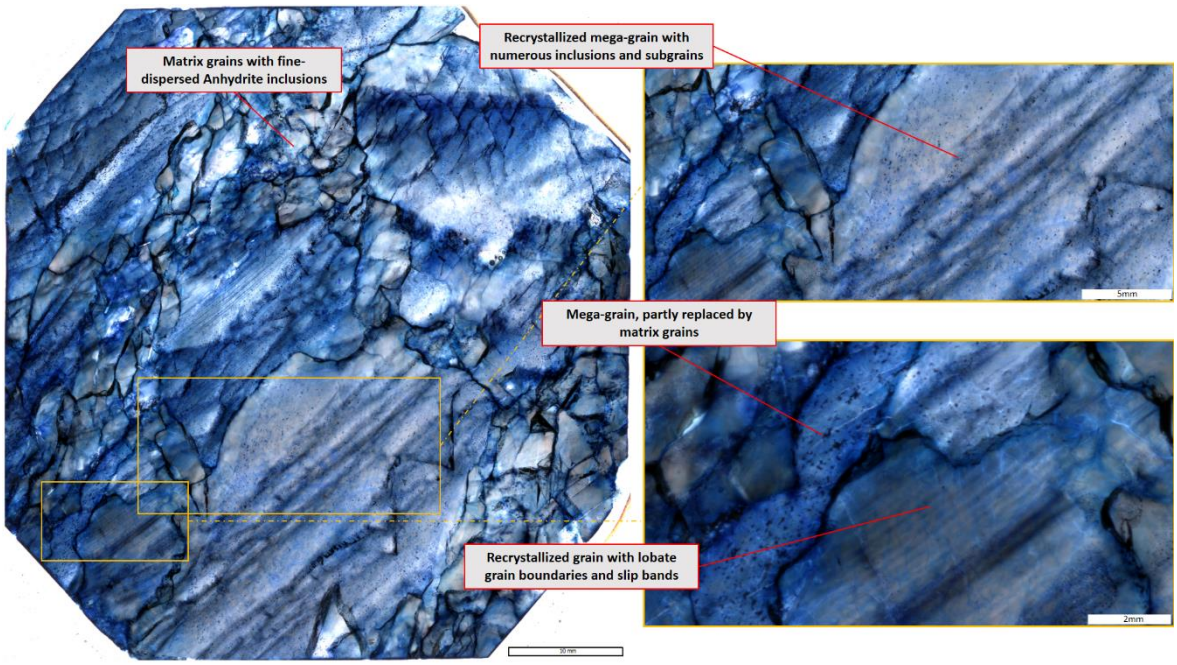

Fig. 2 Transmitted light micrograph (flatbed-scan) of Gamma-irradiated Kristallbrockensalz The inclusion rich mega-grain remnants with subgrains are replaced by strain-induced, fluid-assisted grain boundary migration recrystallization. The surrounding fine-grained Halite deforms by pressure solution and is much weaker during tectonic deformation at low differential stress than the mega-grain, which deform by dislocation creep. Sample ID: ZW_MaP_04g (ZW A2A 8_7_1505.80 (ZEZ2HM)).

Table 1 Overview on samples, subsamples, and analyses

WELL	CORE	CORE BOX	DEPTH TOP	STRATIGRAPHIC UNIT	LITHOCLASS	MAP ID PREFIX	THIN SECTION ID	GRAIN SIZE DIST.	SUBGRAIN SIZE DIST.	BIB-SEM	BROKEN GB	SEM/EDS	POWDER SECOND PHASE %	DEFORMATION MINE	DEFORMATION IFG	PERMEATION
ZW A1A	2	2	452.62	ZEZ2HM	F (G)	ZW_MaP_16	_ts	GSD		_BIB-SEM			_powder		planned	planned
ZW A1A	4	7	959.20	ZEZ2HM	F (G)	ZW_MaP_13	_ts	GSD	SGSD				_powder		planned	planned
ZW A1A	9	1	1518.00	ZEZ3HL	G	ZW_MaP_20	_ts	GSD	SGSD	_BIB-SEM						
ZW A2A	7	9	1467.00	ZEZ2HM	G (F)	ZW_MaP_09	_ts	GSD	SGSD				_powder		ZW_MaP_17_PreT	
ZW A2A	8	7	1505.80	ZEZ2HM	F	ZW_MaP_04_g	_ts							planned		
ZW A2B	1	2	650.80	ZEZ2HL2	G (F)	ZW_MaP_14	_ts	GSD	SGSD	_BIB-SEM						
ZW A3A	1	2	591.90	ZEZ2HL1	H	ZW_MaP_15	_ts	GSD	SGSD	_BIB-SEM			_powder		planned	planned
ZW A3A	2	1	991.00	ZEZ2HL1	H	ZW_MaP_21	_ts	GSD	SGSD						planned	planned
ZW A3A	6	5	1444.50	ZEZ2HL1	H	ZW_MaP_10	_ts	GSD	SGSD			_SEM/EDS				
ZW A4A	5	10	1028.00	ZEZ2HL2	G	ZW_MaP_12	_ts	GSD		_BIB-SEM			_powder		planned ZW2.1	planned
ZW A4A	10	1	1441.00	ZEZ2HL1	G	ZW_MaP_22	_ts	GSD	SGSD	_BIB-SEM	_GB					
ZW A5A	1	9	268.18	ZEZ2HM	G	ZW_MaP_28	_ts	GSD			_GB					
ZW A5A	6	9	1190.47	ZEZ2HM	H	ZW_MaP_11	_ts	GSD	SGSD							
ZW A5A ST01	1	5	1503.26	ZEZ3HL	G	ZW_MaP_07	_ts	GSD	SGSD	_BIB-SEM					ZW_MaP_18_PreT	
ZW A6A	1	8	605.00	ZEZ2HL2	G (F)	ZW_MaP_23	_ts	GSD	SGSD	_BIB-SEM	_GB					
ZW A6A	2	4	1006.30	ZEZ2HL2	F	ZW_MaP_24	_ts	GSD	SGSD							
ZW A6A	6	9	1461.00	ZEZ2HM	F	ZW_MaP_25	_ts	GSD								
ZW A7A	5	2	1294.71	ZEZ2HL1	H	ZW_MaP_26	_ts	GSD	SGSD							
ZW A7A	7	1	1604.00	ZEZ2HL2	G	ZW_MaP_27	_ts	GSD	SGSD			_SEM/EDS				
ZW A7B	1	5	1393.68	ZEZ2HL1	G	ZW_MaP_29	_ts	GSD								
ZW A7B	1	13	1400.88	ZEZ2HL1	G	ZW_MaP_05_g	_ts						_powder	planned		

WELL	CORE	CORE BOX	DEPTH TOP	STRATIGRAPHIC UNIT	LITHOCLASS	MAP ID PREFIX	THIN SECTION ID	GRAIN SIZE DIST.	SUBGRAIN SIZE DIST.	BIB-SEM	BROKEN GB	SEM/EDS	POWDER SECOND PHASE %	DEFORMATION MINE	DEFORMATION IFG	PERMEATION
ZW A7B	2	15	1469.27	P0	G	ZW_MaP_08	_ts	GSD							planned	planned
ZW A8A	1	8	267.39	ZEZ2HL2	F	ZW_MaP_30	_ts	GSD			_GB					
ZW A8A	2	10	542.23	ZEZ2HL2	G	ZW_MaP_02_g	_ts						_powder		planned	
ZW A8A	4	8	1090.63	ZEZ2HM	F	ZW_MaP_31	_ts	GSD			_GB					
ZWD-KNZ-8	1	10	242.70	ZEZ2HL2	F	ZW_MaP_01_g	_ts								ZW_MaP_19_PreT	
ZWD-KNZ-8	5	5	1003.13	ZEZ2HL2	F	ZW_MaP_32	_ts	GSD	SGSD							
ZWD-KNZ-8	13	8	1627.58	ZEZ3HL	H	ZW_MaP_03_g	_ts						_powder		planned	planned
ZWD-KNZ-8	15	6	1795.01	ZEZ3HM	G	ZW_MaP_06	_ts	GSD	SGSD				_powder		planned	planned
ZWD-KNZ-9	2	2	421.95	ZEZ3HM	F	ZW_MaP_33	_ts		SGSD			_SEM/EDS				

Grain size measurements using optical microscopy and image analysis

Determination of grain size and other structural features from micrographs using image analysis is often not trivial. Especially for monomineralic materials, standard image processing like thresholding, but also more sophisticated methods such as watershed segmentation, may lead to erroneous results, due to the very small contrast of grain boundaries in monomineralic rocks, which cannot be segmented easily and thus may lead to overestimating the grain size. Additionally, next to the grain boundaries and subgrain boundaries, we identify a number of other structures in the micrograph, such as second phase inclusions and preparation artifacts, which complicate automated image segmentation. We therefore developed a semi-automated segmentation tool, which allows fast manual segmentation, and allowing the user to confirm a pre-segmentation provided based on thresholding (Fig. 3). The interpretation of grain boundaries was benchmarked by comparing interpretations by two independent experts (Urai and Schmatz), with satisfactory results. Grain size was computed using the circular equivalent diameter *d*. The orientation of the grains was determined by the longest axes of the fitted ellipse, and its aspect ratio to describe the elongation of the grains. Most of the grain boundaries as well as the grains contained second phases, such as fluid inclusions and small Anhydrite grains or grain clusters. We used the segmentation routine to exclude second phases present at the grain boundary from - and to include second phases present inside the grains to the measured area of the grain. Grains that touched the edges of the images or thin section were not measured. The sections were cut parallel to the slabs, and perpendicular to the longest axis of the grain, as far as this was visible when cutting the slabs from the core (we realize that elongated grains may have a small effect on rates of pressure solution creep, but this effect is outside the scope of the present analyses).

Subgrain size measurements using optical microscopy and image analysis

We use the subgrain size as a piezometer using the laboratory-calibrated relation of the average subgrain size and differential stress. The appearance of the subgrains is dependent on the quality of thin section surface preparation, on the orientation of the grains, and the misorientation of the subgrains. However, the etching is very sensitive to subgrains, which has been verified by EBSD analyses, so that the etching technique is inferred to decorate all subgrain boundaries in Halite. Because of the artefacts, there is the possibility of misinterpretation; thus, the segmentation task is again not trivial. Starting from a benchmark comparing interpretation of two independent operators, we used the same semi-automated segmentation tool as used for the grain segmentation (Fig. 3). The subgrain size reported as the circular equivalent diameter (D) of the segmented subgrains. The pixel resolution of the interpreted micrographs was 0.69µm. For each thin section, we selected several grains with subgrains at different locations within the thin section (see the Appendix A for the exact locations of the subgrain size measurements from reflected light micrographs). We followed the rule to segment only subgrains, which were visible as closed polygons and that were not connected to high-angle grain boundaries. Subgrains that touched the edges of the images were not measured.

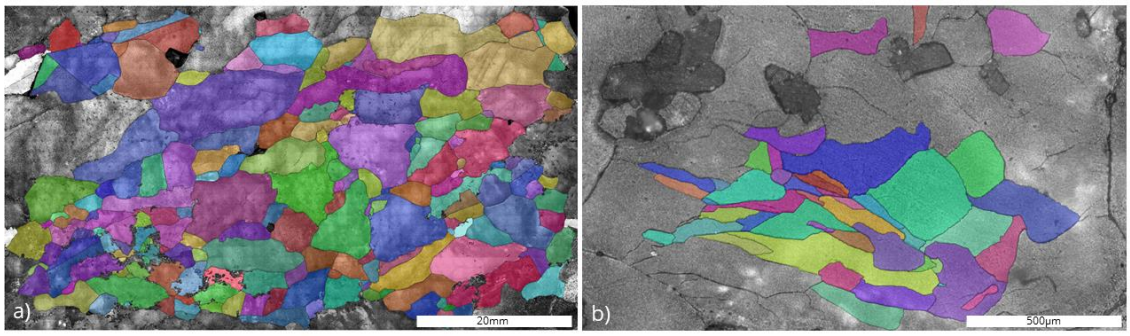

Fig. 3 Reflected light micrograph with (a) grain and (b) subgrain segmentation. Each individual grain/subgrain segmentation has a different color. Sample ID is ZW A5A ST01 1_5_1503.26m (ZEZ3HL) / ZW_MaP_07.

BIB-SEM

Broad Ion Beam polishing (BIB, Fig. 4) is a preparation technique, which allows preparing smooth and dust-free sample surfaces, by removing some of the mechanical damage using Argon-Ion sputtering. This way we are able to image microstructures using SEM that could be hidden or misinterpreted because of the mechanical damage caused by cutting and grinding.

From the sub-samples, up to 100 µm of material was removed by using the JEOL BIB cross-section polisher (SM 09010). A titanium mask is put on the top of the sample, leaving about 100 µm of material uncovered which will be bombarded with Argon ions. The sample is oscillating during the ion milling to prevent curtaining of the polished section. Typically, the JEOL cross-section polisher produces a pseudo-Gaussian shaped polished surfaces covering an area of 1 – 2mm^2 when operating for 8 hours at 6 kV and 150 µA. The BIB cross-section is a flat, planar surface with a minimum relief of ±5 nm over 1 µm^2.

BIB-SEM was used to study the grain boundary structure of selected grain boundaries in selected samples as well as morphology and distribution of the second phase inclusions.

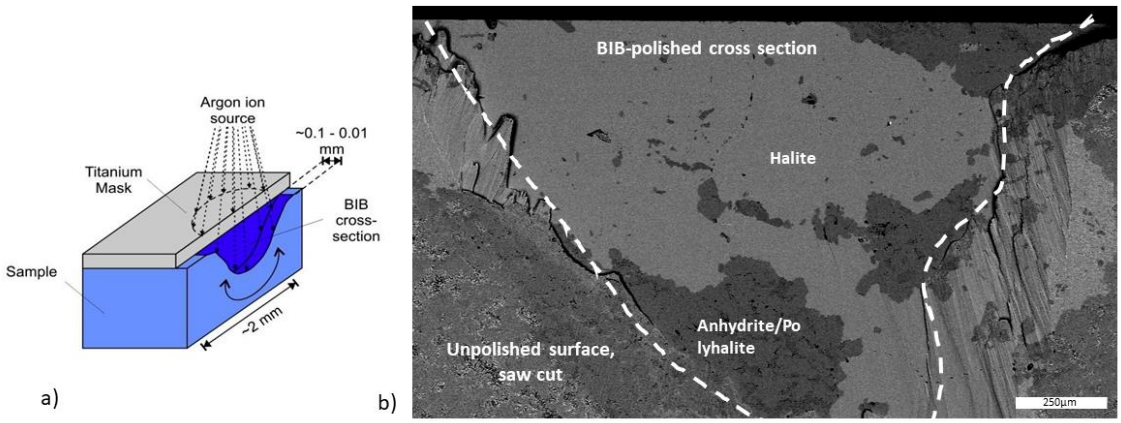

Fig. 4 a) Sketch of BIB cross-section polishing in the JEOL BIB. b) BSE Micrograph showing of the BIB-polished cross-section. Sample ID is ZWD_A2B_1_2_651m

Grain boundary structure

We studied the grain boundary structure in all samples using OM in reflected light and in transmitted light, usually with partly crossed polarizer and analyser, allowing studying the isotropic Halite grains as well as the birefringent Anhydrite grains, often located inside grain boundaries and within grains, at the same time, using the microscope settings as described above.

High-resolution SEM on Halite polycrystals, broken along grain boundaries, was used to investigate grain surface morphology and imprints of fluid inclusion arrays in selected samples from different depths and litho-classes (Fig. 5a). Furthermore, we used BIB to prepare sample cross-sections allowing investigating the grain boundary structure at high-magnification in the SEM for selected samples from different depths and litho-classes (Fig. 5b). Further information on grain boundary structure was collected by SEM on etched thin section surfaces (Fig. 5c).

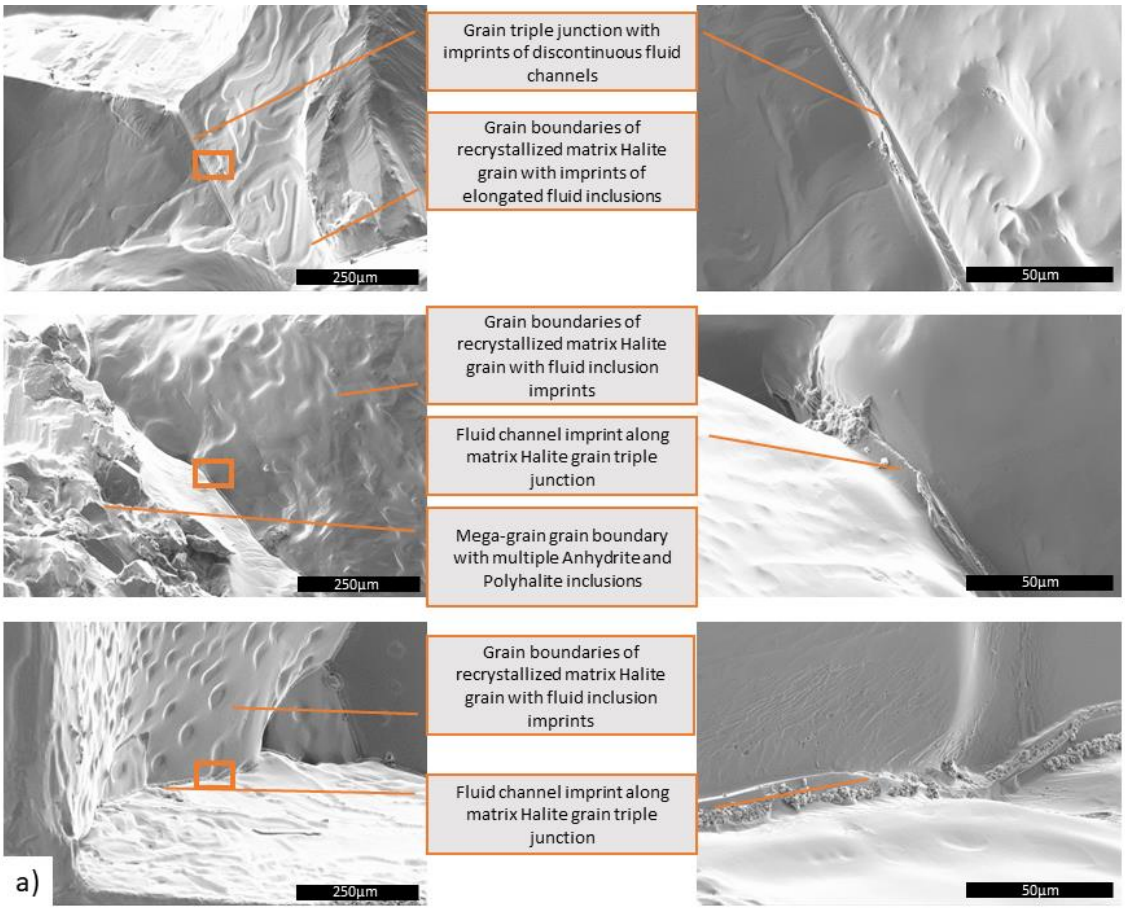

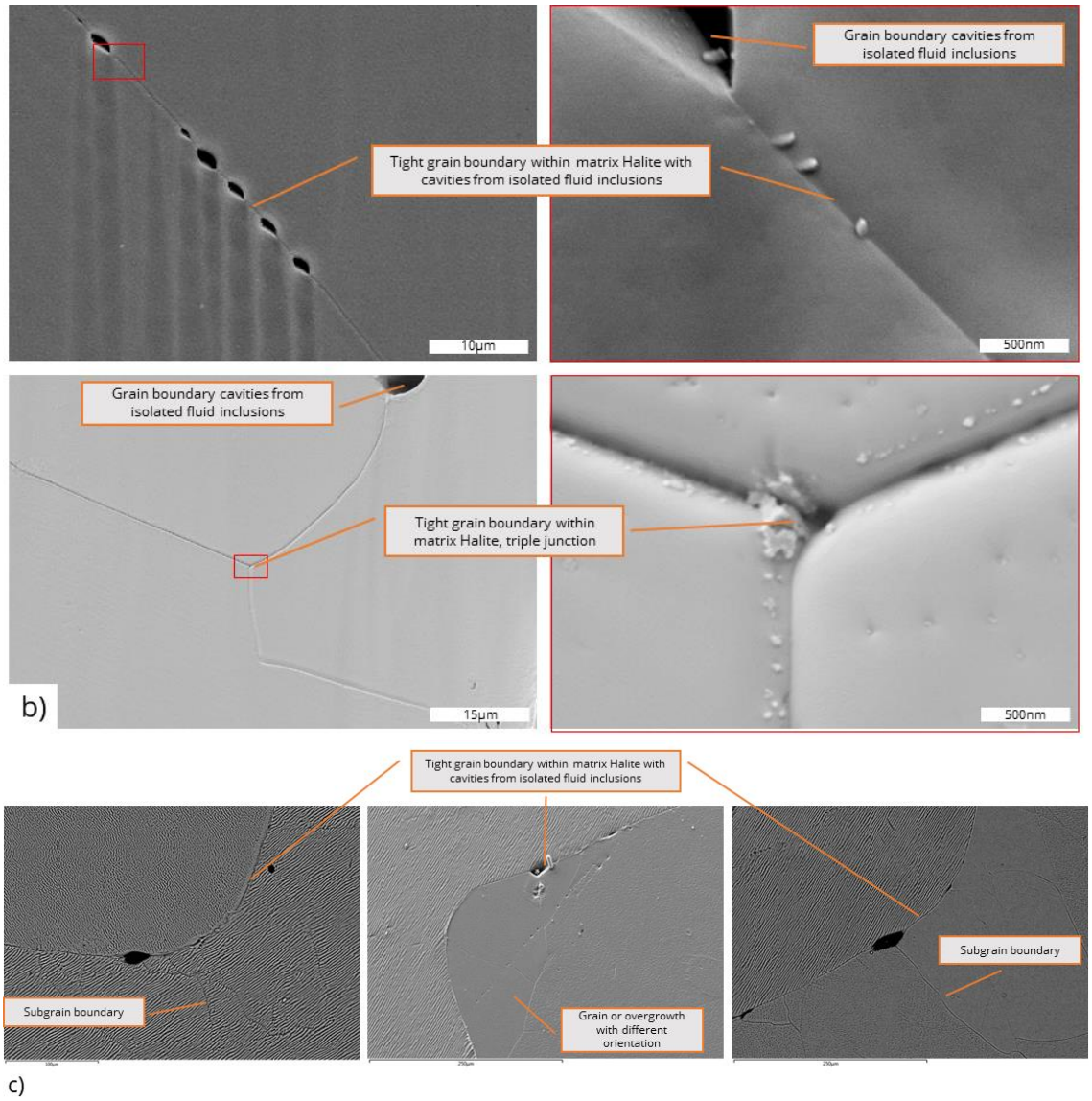

Fig. 5 SEM micrographs showing the grain boundary structure. a) grain boundary surfaces of Halite polycrystals broken along the grain boundaries (right image is close-up of the center of the right image, Sample IDs:ZW_MaP_28 (ZWD-A5A_1_9_268.18) and ZW_MaP_30 (ZWD-A8A_1_8_267.39), b) BIB-prepared cross-sections of grains boundaries showing tight grain boundary with fluid inclusion cavities (Sample IDs ZW_MaP_16 (ZWD-A1A 2_2_0452.62) and ZW_MaP_23 (ZWD-A6A_1_8_605.00)), c) etched thin section surface showing tight grain boundaries with fluid inclusion cavities. Surface pattern with different orientation indicates differences in lattice orientation of adjacent grains. Sample ID: ZW_MaP_27 (ZWD-A7A_7_1_1604.00).

Second phase impurities

Bulk Analysis of second phase impurities

The bulk content of non-soluble or weakly soluble mineral phases was determined from 20 core pieces selected for deformation and permeation experiments. Experimental setup at IfG (Institut für Gebirgsmechanik GmbH, Leipzig) required grinding down the core pieces to a defined diameter suitable for the testing apparatus. The resulting powder was sent to MaP for bulk analyses. A fraction of the powder was dissolved and the insoluble content was measured using the following protocol for each of the powder samples: 20 g were dissolved in 200 ml deionized water for 30 min. at room temperature. The solution was stirred regularly. The solution was filtered and the filtrate weighed with a precision balance.

Subsequent SEM-EDS analysis of the insoluble confirmed that the Halite was dissolved and not present in the residue. The volumetric content was calculated using the density of Halite and Anhydrite, as the dominant second phase mineral, neglecting the contribution of other minerals present with minor proportions such as Polyhalite and Gypsum (presumably formed by hydration of Anhydrite during the dissolution). Mineralogy and shape of the insoluble particles was studied using SEM/EDS (Fig. 6).

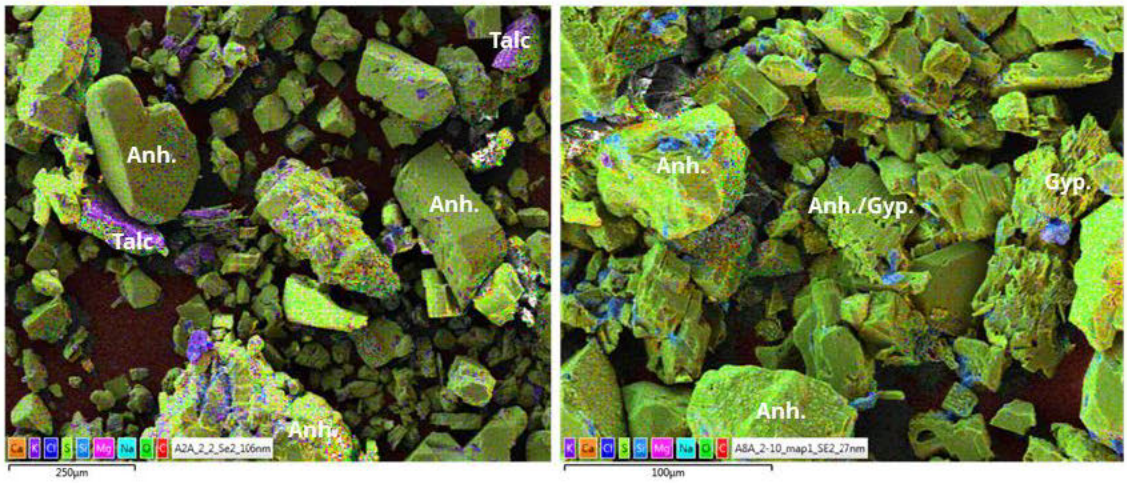

Fig. 6 SEM micrographs (SE2 with EDS overlay) showing the morphology of the insoluble grains. The predominant phase is Anhydrite with minor amounts of talc. The porous and platy grain morphology indicates that Anhydrite has partially hydrated to Gypsum. Sample IDs: ZW_MaP_09 (ZWD-A2A 7_9_1467.00) and ZW_MaP_02_g (ZWD-A8A_2_10_0542.23).

Microscopic analyses of second phase impurities

The nature and distribution of the second phase impurities was studied using OM in all thin section samples, SEM on selected thin section samples, as well as on selected BIB-prepared samples. High-resolution EDS-mapping was used to assess the chemical composition of the second phases. BIB-SEM was used to assess the microporosity of the second phase Anhydrite as well as the related pore-fillings (Fig. 7, Fig. 8, Fig. 9, and Fig. 10).

X-Ray diffraction analysis (XRD)

Further to the spatially resolved chemical analysis using EDS, two samples from different depths and litho-classes (; ZW_MaP_26, ZWD-A7A_1294.71m; ZW_MaP_30, ZWD-A8A_1_8_267.39m) that contained a visibly large proportion of Anhydrite were measured using XRD (device specification: Bruker D2 Phaser).

Table 2 Result XRD analyses.

	ZW_MAP_26	ZW_MAP_30
HALITE	86 (±3,0) %	76 (±6,0) %
POLYHALITE	5.5(±1,3) %	5.3(±1,5) %
ANHYDRITE	8.6 (±1,6) %	19 (±4,0) %

Results

Summary of microtectonic observations

The microstructural investigations clearly show the three structural elements: (i) mega-grains of Halite up to 20 cm long (slab scale) and up to 2 cm thick (slab-scale), fine grained Halite matrix, and thin (few mm thick) folded and boudinaged layers of fine-grained Anhydrite (e.g., Fig. 1). The mega-grains are aligned subparallel to bedding, and the fine-grained Halite matrix forms a variable fraction of the rock. This was investigated in ZW1.1.

Matrix Halite grain size is commonly between 0.6 and 2.5mm consisting of primary grains with chevron inclusions, small relict grains of deformed mega-grains, and slightly elongated grains with occasional subgrains (e.g., Fig. 1, Fig. 2, and Fig. 3). The second phase content of the rock salt is commonly very low (Table 3) and dispersed Anhydrite/Polyhalite grains in the Halite matrix are often concentrated along formed Halite grain boundaries. In the vicinity of Anhydrite bands, large, idiomorphic Anhydrite grains are found within the matrix grains and within the matrix-grain boundaries. A few locations show pinning of the grain boundaries of the recrystallized grains by the second phase inclusions (Fig. 7).

Grain boundaries in Halite (in-situ) are healed and contain isolated fluid inclusions (water, gas, hydrocarbons), with water content inferred to be below 1% (Fig. 5 and Fig. 8). Some grain boundaries show efflorescence of Halite after sample preparation (Fig. 7). The rock salt in the core thus contains very little if any connected porosity and is inferred to be close to impermeable at this scale. The Halite mega-grains contain the characteristic Anhydrite-Brine inclusions also reported in other studies (Fig. 9).

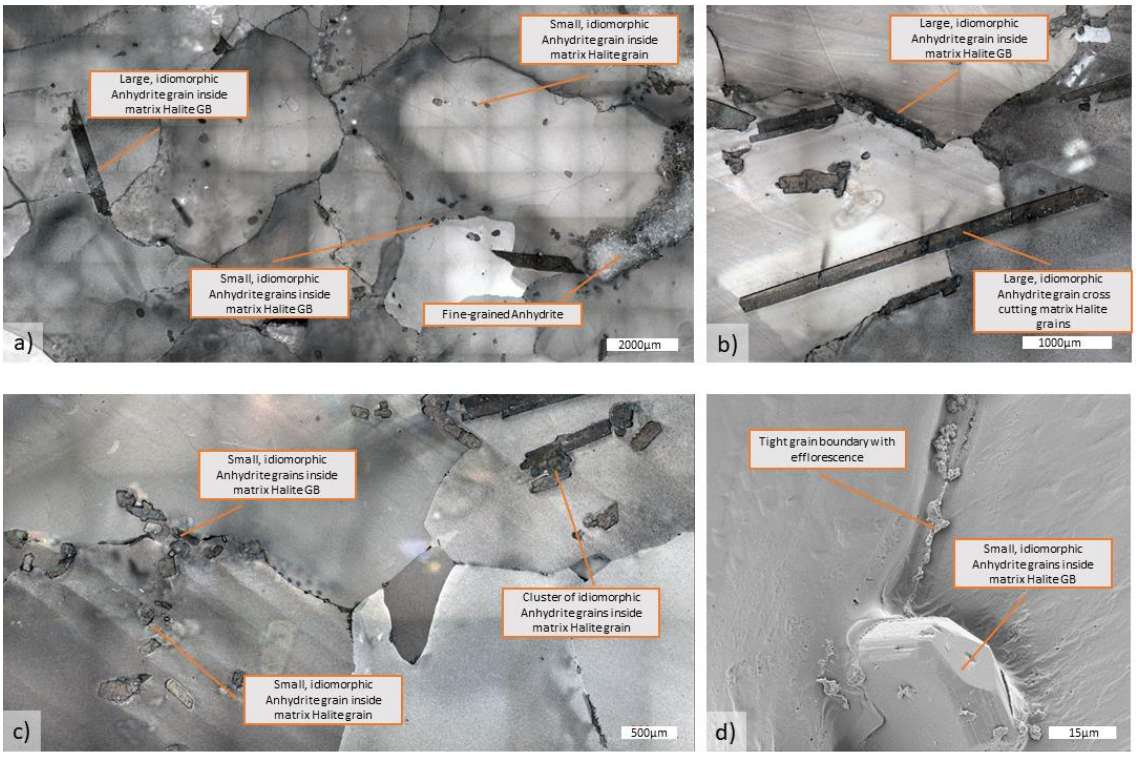

Fig. 7 Reflected light (a-c) and SEM (d) micrographs and showing matrix Halite with second phase impurities. The second phase content of the rock salt is very low and dispersed Anhydrite/Polyhalite grains in the Halite matrix are often concentrated along formed Halite grain boundaries. Sample IDs: ZW_MaP_14 (ZWD-A2B 1_2_0650.80m), ZW_MaP_22 (ZWD-A4A_10_1_1441.00m), and ZW_MaP_31 (ZWD-A8A_4_8_1090.63m).

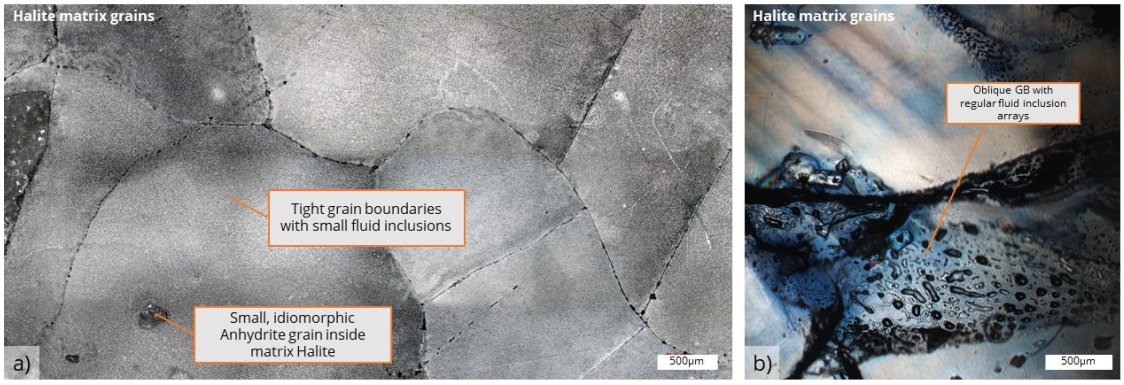

Fig. 8 a) Reflected light micrograph of the fine grained Halite matrix in Kristallbrockensalz. Grain boundaries are tight with unconnected microporosity, indicating exceedingly low permeability. The microstructure shows fluid-assisted grain boundary migration recrystallization. Sample ID is: ZW_MaP_10 (ZWD-A3A 6_5_1444.50), b) Transmitted light micrograph of Gamma-irradiated sample showing oblique grain boundaries in matrix Halite with equilibrated fluid inclusion arrays. Sample ID is ZW_MaP_05_g (ZWD-A7B 1_13_1400.88).

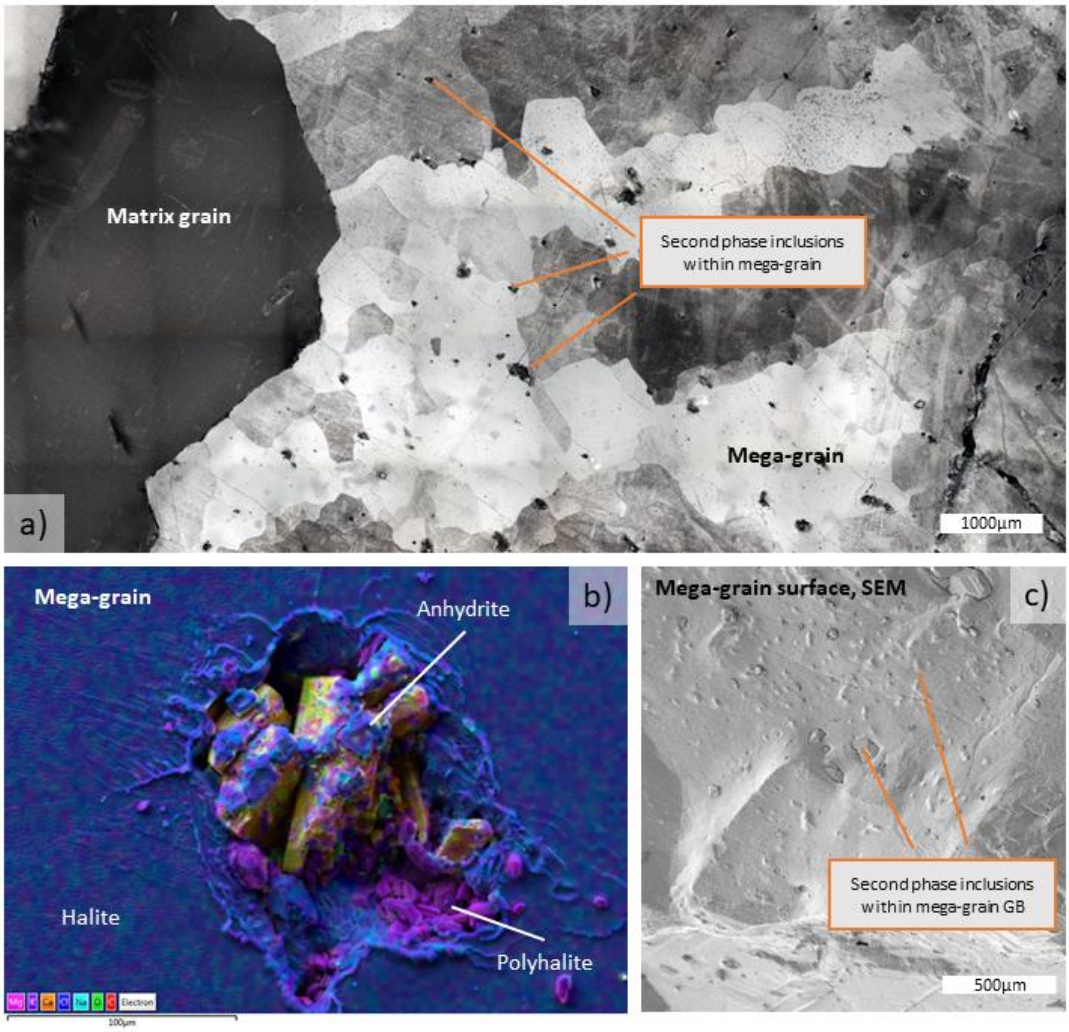

Fig. 9 a) Reflected light micrograph showing Anhydrite/Polyhalite inclusions inside Halite-mega-grain. b) SEM/EDS layered image of thin section sample showing Anhydrite/Polyhalite inclusions inside Halite mega-grain. The solid inclusions embedded into a fluid inclusion cavity. See legend in the left corner for the elemental composition. c) SEM micrograph of mega-grain grain boundary surface with second phase inclusions

Further observations of second phase impurities

The content and distribution of the second phase impurities were determined by bulk measurements and microscopy. XRD measurements on selected samples containing a visibly large amount of second phases (Table 2) confirmed that the first dominant second phase was Anhydrite, which occurred together with small amounts of Gypsum (Fig. 6), presumably formed after sampling. The second dominant second phase was Polyhalite. SEM imaging and chemical EDS analysis of thin-section samples (Fig. 10a-c) and samples prepared with BIB (Fig. 10d-e) showed that Anhydrite and Polyhalite alternated in the areas rich in second phases, which generally formed thin (thickness about 1-5 mm), folded and boudinaged bands that often bordered on the mega-grains. Anhydrite was often porous (see e.g. Fig. 10d-e), with the porosity occasionally filled with Polyhalite and small amounts of clay (see Appendix). Anhydrite/Polyhalite layers and fragments were often surrounded by large idiomorphic Anhydrite or Polyhalite grains up to one millimetre in size (Fig. 10c). In addition to the thin layers, the second phases occurred within the matrix Halite, along the grain boundaries and within the recrystallized grains. Here, the Anhydrite and Polyhalite grains were generally idiomorphic to hypidiomorphic and occurred as isolated grains of different sizes or in the form of grain clusters (Fig. 7). Grain boundary pinning caused by small (5-200 µm) Anhydrite/Polyhalite grains located at the matrix Halite grain boundaries was occasionally observed (e.g., Fig. 7.

The content of insoluble substances (Table 3, Fig. 6 and Fig. 11) ranged from 2.7 to 19.1 Vol.%, with the largest amount of insolubles found in litho-class H. (see ZW1.1 final report for the characteristics of the litho-classes).

Table 3 Insoluble content from dissolved powder.

WELL/CORE	SAMPLE	VOL% INSOLUBLE
KNZ-8/15-6	/ZW_MaP_06	8.20%
A3A/2-1	/ZW_MaP_15	19.60%
KNZ8/13-8	/ZW_MaP_03_g	15.70%
A8A/2-10	/ZW_MaP_02_g	6.40%
A5A ST01/1-5	ZW_MaP_18_PreT/ZW_MaP_07	5.30%
A2A/7-9	ZW_MaP_17_PreT/ZW_MaP_09	3.30%
A1A/2-2	/ZW_MaP_16	7.20%
A4A/5-10	/ZW_MaP_12	7.60%
A1A/4-7	/ZW_MaP_13	2.70%

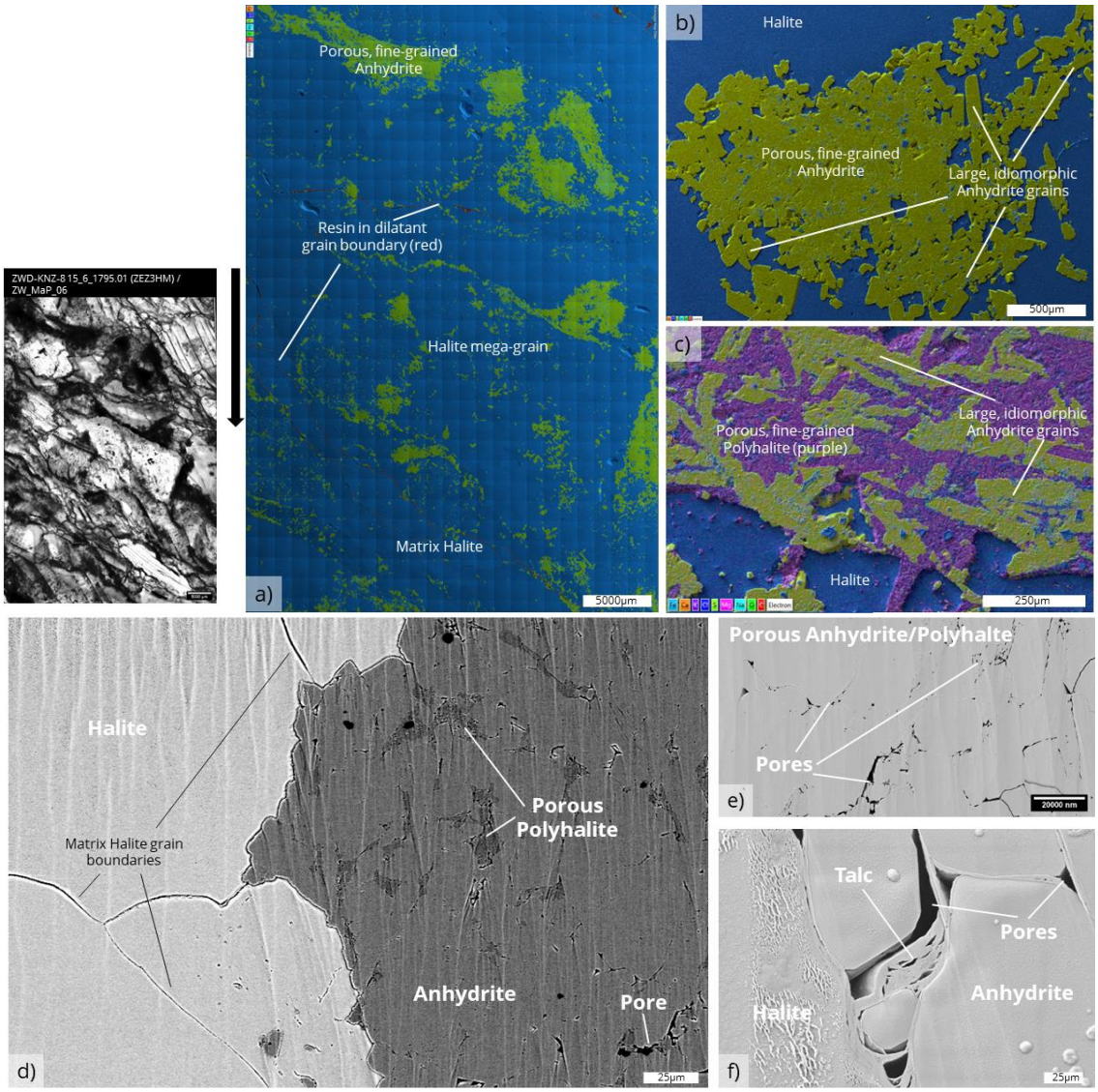

Fig. 10 a) SEM/EDS layered image of a thin section sample showing folded, fine-grained Anhydrite layer with large, elongated Polyhalite grains. b) The Anhydrite is porous and the porosity is filled with Polyhalite. c) BIB-SEM micrograph showing porous Polyhalite interbedded with idiomorphic Anhydrite grains. d-f BIB-SEM micrographs showing second phase Anhydrite and Polyhalite with porous Polyhalite with clay (Talc) filling inside the pore space.

Summary of quantitative analyses

We measured microstructural features of 30 core sections using for each of them a selection of the above-described microanalytical methods (Table 1). In Fig. 11 we summarize the quantitative results of our measurements regarding the recrystallized Halite fraction in relation to the litho-classes defined in ZW1.1 (Fig. 11a) regarding the median grain size (Fig. 11b), the subgrain size (Fig. 11c) and the derived differential stress (Fig. 11d), the average grain aspect ratio derived from the fitted ellipse (Fig. 11e), as well as the insoluble content (Fig. 11f) versus the depths of the core samples. The results of the presented measurements will be described in the following sections.

Grain size distribution

As described above (e.g., Fig. 1), the samples consisted of matrix Halite grains and Halite mega-grains. Since the size of the Halite mega-grains could not be measured on the thin section scale, as they usually exceeded the size of the thin section, we only measured the size of the matrix Halite grains. This measurement also includes small remnants of mega-grains that were part of the Halite matrix (e.g., Fig. 3). In total, we measured 10217 matrix Halite grains in all thin sections. The average number of grains measured per thin section was 409 (Table 4, min. 143, max. 664). The majority of the grain size distributions correspond to a lognormal distribution (Fig. 12). The minimum median grain size *d* measured in all distributions was 0.6 mm and the maximum was 2.7 mm. We measured an average median grain size of all distributions of 1.2 mm with an average standard deviation of 2.9mm. There was no trend of decrease in grain size with depth among the samples and no trend of grain size development among the different lithologic units or litho-classes.

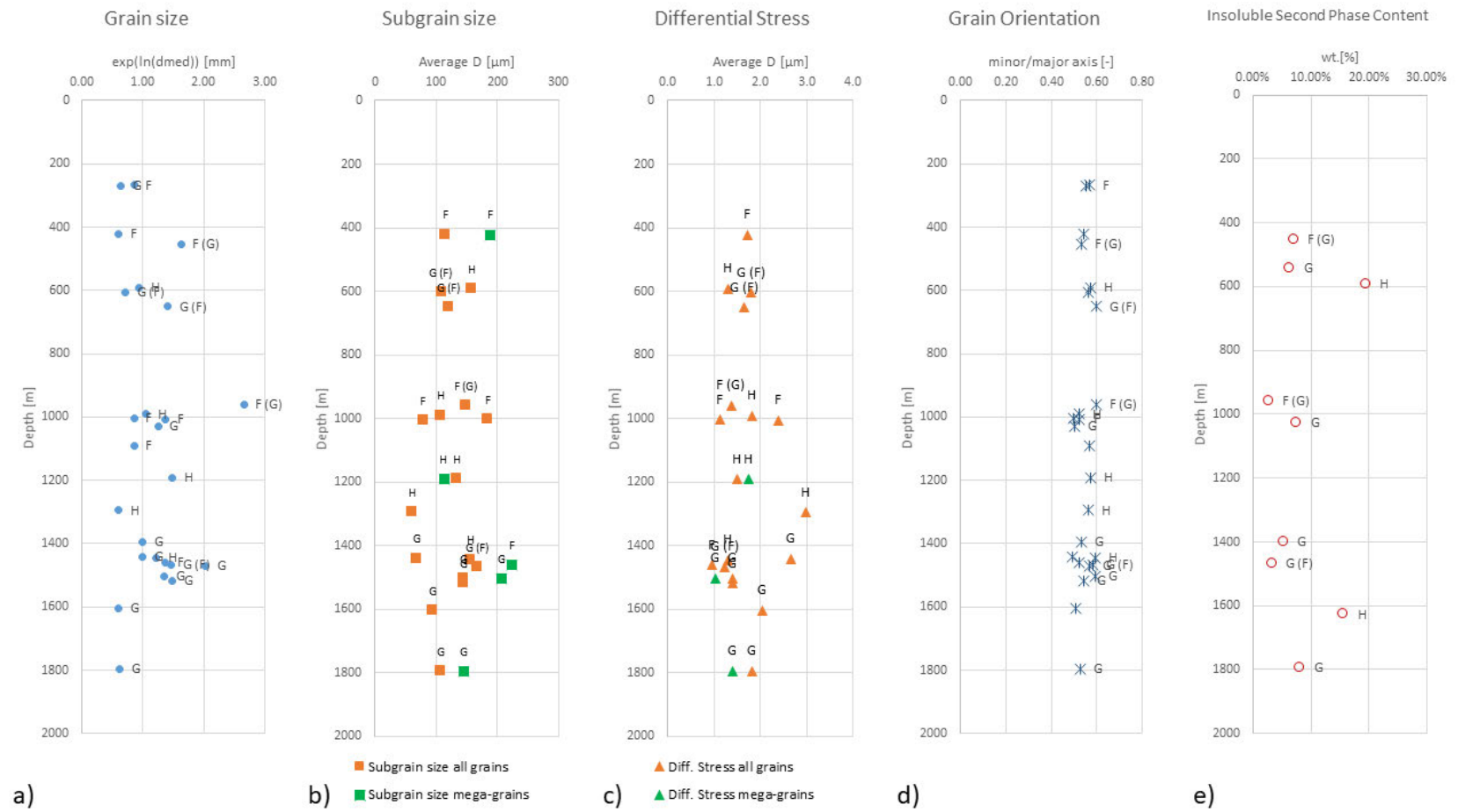

Fig. 11 Graphs showing a) the average median grain size derived from the log-normal distribution, b) the average subgrain size, c) the derived differential stress, d) the grain aspect ratio, and e) the content of insoluble second phases versus the depth. Labels (F, G, H) indicate the litho-class.

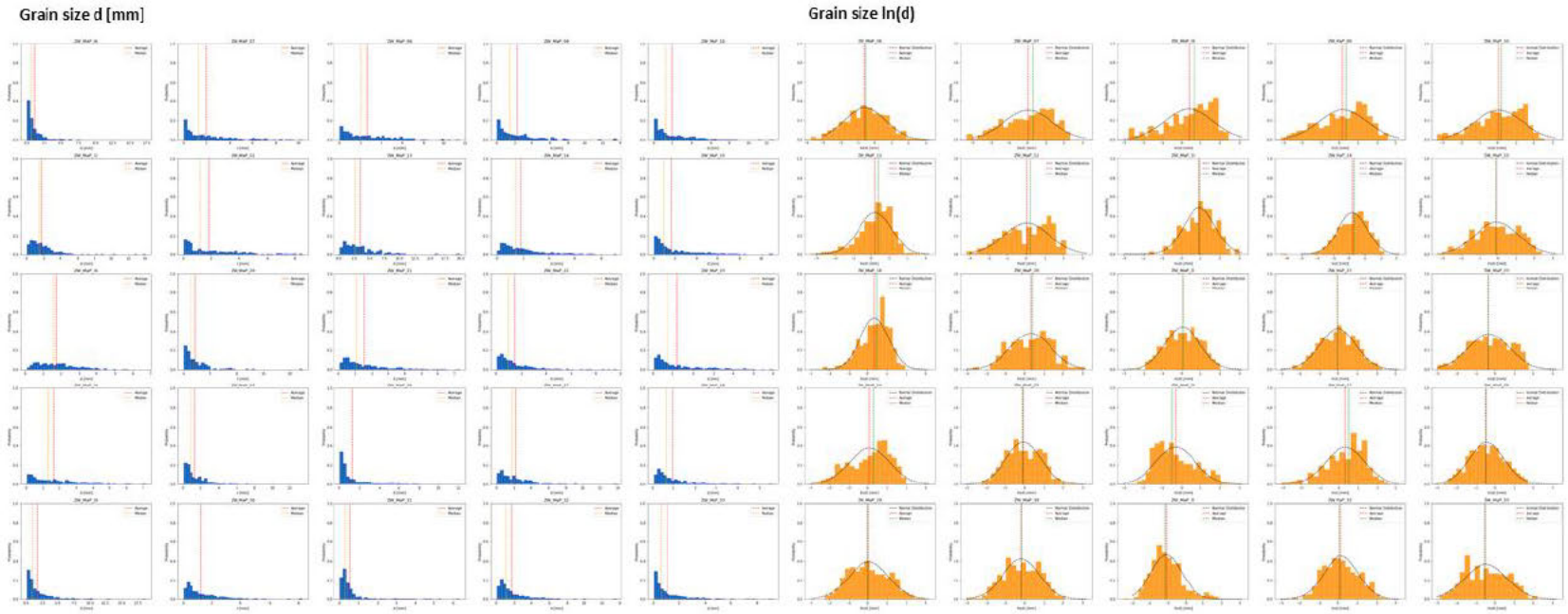

Fig. 12 Histograms showing the grain size distribution for the thin section samples (left, blue) and the lognormal grain size distribution (right, orange)

Table 4 Overview grain size statistics.

							GRAIN SIZE D							GRAIN SIZE LN(D)							
WELL	CORE	CORE BOX	DEPTH TOP	STRATIGRAPHIC UNIT	LITHOCLASS	THIN SECTION	COUNT	MIN [MM]	MAX [MM]	MEDIAN [MM]	AVERAGE [MM]	STD_DEVIATION [MM]	MODE [MM]	COUNT	MIN	MAX	MEDIAN	AVERAGE	STD_DEVIATION	MODE	EXP(MEDIAN) [MM]	EXP(STD_DEVIATION) [MM]
ZW A1A	2	2	452.62	ZEZ2HM	F (G)	ZW_MaP_16	626	0.10	6.71	1.62	1.77	1.11	0.61	626	-2.34	1.90	0.48	0.34	0.74	0.73	1.62	2.10
ZW A1A	4	7	959.20	ZEZ2HM	F (G)	ZW_MaP_13	156	0.19	19.78	2.66	3.46	2.86	0.63	156	-1.65	2.98	0.98	0.93	0.82	0.64	2.66	2.26
ZW A1A	9	1	1518.00	ZEZ3HL	G	ZW_MaP_20	170	0.07	22.25	1.48	2.31	2.72	0.28	170	-2.70	3.10	0.39	0.32	1.06	-0.11	1.48	2.88
ZW A2A	7	9	1467.00	ZEZ2HM	G (F)	ZW_MaP_09	143	0.04	13.48	1.47	2.29	2.45	1.97	143	-3.13	2.60	0.38	0.18	1.28	0.25	1.47	3.61
ZW A2A	8	7	1505.80	ZEZ2HM	F	ZW_MaP_04_g																
ZW A2B	1	2	650.80	ZEZ2HL2	G (F)	ZW_MaP_14	664	0.01	9.14	1.41	1.81	1.50	0.37	664	-4.32	2.21	0.34	0.23	0.91	-0.22	1.41	2.48
ZW A3A	1	2	591.90	ZEZ2HL1	H	ZW_MaP_15	404	0.04	11.08	0.93	1.72	1.87	0.23	404	-3.29	2.40	-0.07	-0.06	1.17	-1.35	0.93	3.22
ZW A3A	2	1	991.00	ZEZ2HL1	H	ZW_MaP_21	445	0.10	7.30	1.06	1.54	1.34	0.29	445	-2.35	1.99	0.05	0.06	0.90	-0.48	1.06	2.45
ZW A3A	6	5	1444.50	ZEZ2HL1	H	ZW_MaP_10	365	0.04	12.57	1.22	2.01	2.04	0.05	365	-3.28	2.53	0.20	0.06	1.30	-0.18	1.22	3.67
ZW A4A	5	10	1028.00	ZEZ2HL2	G	ZW_MaP_12	394	0.04	8.49	1.25	1.87	1.83	0.19	394	-3.15	2.14	0.22	0.04	1.20	0.85	1.25	3.33
ZW A4A	10	1	1441.00	ZEZ2HL1	G	ZW_MaP_22	514	0.09	9.60	1.00	1.48	1.46	0.38	514	-2.36	2.26	0.00	-0.02	0.93	0.37	1.00	2.52
ZW A5A	1	9	268.18	ZEZ2HM	G	ZW_MaP_28	500	0.07	5.64	0.63	0.97	0.96	0.41	500	-2.66	1.73	-0.47	-0.44	0.91	-0.89	0.63	2.49
ZW A5A	6	9	1190.47	ZEZ2HM	H	ZW_MaP_11	614	0.03	14.00	1.48	1.74	1.45	0.66	614	-3.35	2.64	0.39	0.22	0.91	0.85	1.48	2.47
ZW A5A ST01	1	5	1503.26	ZEZ3HL	G	ZW_MaP_07	299	0.04	10.31	1.35	2.02	2.09	0.15	299	-3.29	2.33	0.30	0.04	1.30	0.93	1.35	3.68
ZW A6A	1	8	605.00	ZEZ2HL2	G (F)	ZW_MaP_23	463	0.05	5.97	0.72	1.22	1.21	0.22	463	-2.95	1.79	-0.33	-0.31	1.07	-0.20	0.72	2.93
ZW A6A	2	4	1006.30	ZEZ2HL2	F	ZW_MaP_24	427	0.05	7.15	1.36	1.70	1.45	0.14	427	-2.94	1.97	0.31	0.08	1.06	0.96	1.36	2.89
ZW A6A	6	9	1461.00	ZEZ2HM	F	ZW_MaP_25	501	0.11	13.31	0.90	1.40	1.43	0.44	501	-2.25	2.59	-0.11	-0.07	0.91	-0.83	1.36	2.89
ZW A7A	5	2	1294.71	ZEZ2HL1	H	ZW_MaP_26	472	0.10	12.06	0.60	1.32	1.69	0.30	472	-2.34	2.49	-0.51	-0.30	1.03	-1.03	0.60	2.80

							GRAIN SIZE D							GRAIN SIZE LN(D)							
WELL	CORE	CORE BOX	DEPTH TOP	STRATIGRAPHIC UNIT	LITHOCLASS	THIN SECTION	COUNT	MIN [MM]	MAX [MM]	MEDIAN [MM]	AVERAGE [MM]	STD_DEVIATION [MM]	MODE [MM]	COUNT	MIN	MAX	MEDIAN	AVERAGE	STD_DEVIATION	MODE	EXP(MEDIAN) [MM]	EXP(STD_DEVIATION) [MM]
ZW A7A	7	1	1604.00	ZEZ2HL2	G	ZW_MaP_27	200	0.05	13.83	1.68	2.15	1.94	0.21	200	-3.10	2.63	0.52	0.33	1.03	1.24	0.60	2.80
ZW A7B	1	5	1393.68	ZEZ2HL1	G	ZW_MaP_29	459	0.11	18.74	1.00	1.74	2.03	0.23	459	-2.23	2.93	0.00	0.04	1.01	-1.45	1.00	2.76
ZW A7B	1	13	1400.88	ZEZ2HL1	G	ZW_MaP_05_g																
ZW A7B	2	15	1469.27	P0	G	ZW_MaP_08	189	0.06	11.44	2.02	2.62	2.35	1.11	189	-2.75	2.44	0.70	0.40	1.25	1.45	2.02	3.50
ZW A8A	1	8	267.39	ZEZ2HL2	F	ZW_MaP_30	427	0.00	8.25	0.85	1.26	1.21		427	-3.00	2.11	-0.16	-0.18	0.94	-0.88	0.85	2.57
ZW A8A	2	10	542.23	ZEZ2HL2	G	ZW_MaP_02_g																
ZW A8A	4	8	1090.63	ZEZ2HM	F	ZW_MaP_31	427	0.05	8.25	0.23	1.27	1.21	0.23	513	-3.45	1.84	-1.13	-1.07	0.86	-1.37	0.85	2.57
ZWD-KNZ-8	1	10	242.70	ZEZ2HL2	F	ZW_MaP_01_g																
ZWD-KNZ-8	5	5	1003.13	ZEZ2HL2	F	ZW_MaP_32	499	0.10	13.57	1.09	1.71	1.66	0.40	499	-2.34	2.61	0.09	0.15	0.88	0.29	0.85	2.57
ZWD-KNZ-8	13	8	1627.58	ZEZ3HL	H	ZW_MaP_03_g																
ZWD-KNZ-8	15	6	1795.01	ZEZ3HM	G	ZW_MaP_06	457	0.02	17.27	0.61	1.11	1.61	0.08	457	-3.75	2.85	-0.50	-0.57	1.20	-1.84	0.61	3.32
ZWD-KNZ-9	2	2	421.95	ZEZ3HM	F	ZW_MaP_33	402	0.06	9.22	0.61	1.09	1.25	0.23	402	-2.86	2.22	-0.50	-0.48	1.08	-1.40	0.61	2.95

Grain shape and orientation

Matrix grains were usually slightly elongated with aspect ratios (width/length) from the fitted ellipse ranging from 0.49 to 0.60 (Fig. 11) with very small variation and no trend regarding the sample depths. The average aspect ratio (width/length) was 0.55. The orientation of the grains was usually vertical to sub-vertical, following the orientation of the mega-grains when present, i.e., the bedding (Fig. 13).

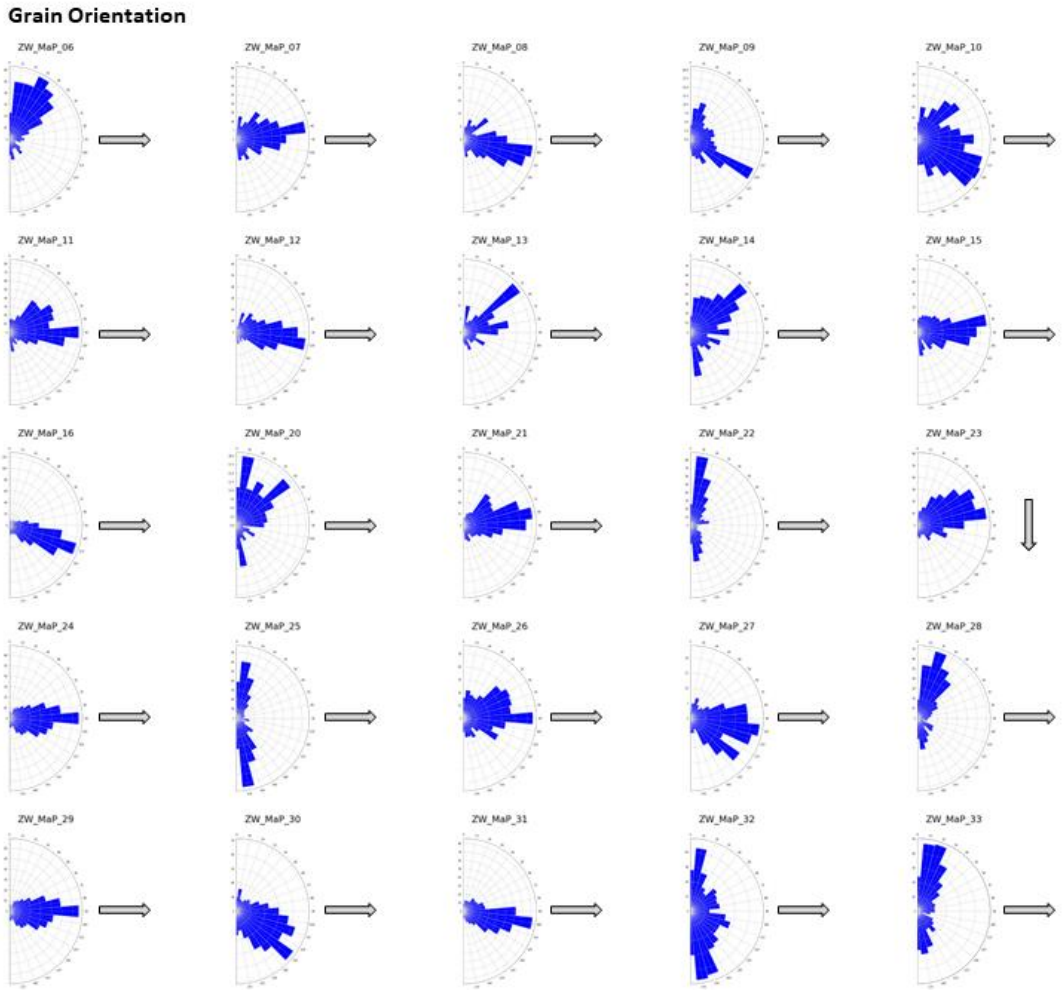

Fig. 13 Rose diagrams showing the orientation of the Halite matrix grains. Arrow indicated the orientation of the core piece.

Subgrain size distribution / Piezometry

We measured in total 10327 subgrains in all thin sections (Table 5), with an average number of 607 per thin section. The average subgrain size for all samples was 124µm. The smallest average subgrain size measured was 61µm and the maximum average subgrain size was 185µm. This result represents the subgrain sizes measured in both types of grains, the recrystallized matrix Halite grains as well as the mega-grains. The average subgrain size within the Halite mega-grains was 175µm and was on average slightly larger than the average subgrain size within all grains. All subgrain size distributions were lognormal (Fig. 14, see Appendix for summary of the distributions of the subgrain sizes for matrix Halite grains and mega-grains). The subgrain size statistics for each individual thin section is given in the Appendix A. Overall, a clear trend of decreasing subgrain size versus the depth was not observable (Fig. 11).

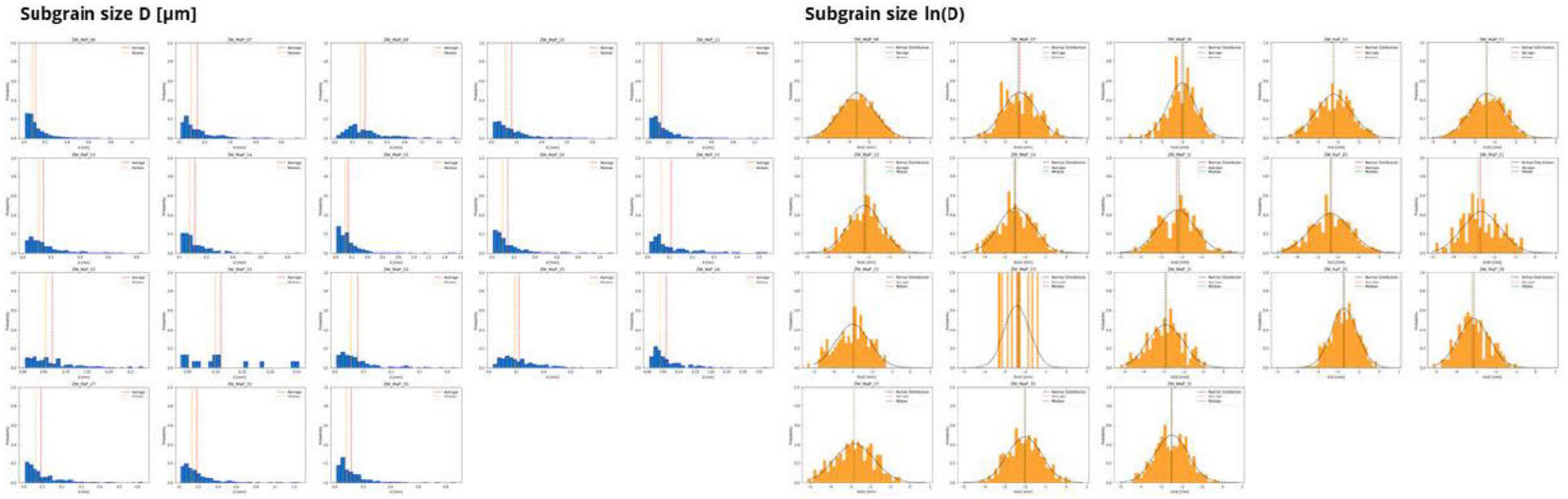

Fig. 14 Overview of subgrain size distributions for all subgrains measured in the thin section samples. (See the Appendix for individual overviews for subgrain sizes measured in mega-grains and matrix grains.

Table 5 Overview subgrain size statistics and derived differential stress

		ALL GRAINS							MEGA-GRAINS							DIFFERENTIAL STRESS ALL GRAINS				DIFFERENTIAL STRESS MEGA GRAINS			
DEPTH TOP	THIN SECTION	NUMBER OF GRAINS	MIN [µM]	MAX [µM]	MEDIAN [µM]	AVERAGE [µM]	STD_DEVIATION [µM]	MODE [µM]	NUMBER OF GRAINS	MIN [µM]	MAX [µM]	MEDIAN [µM]	AVERAGE [µM]	STD_DEVIATION [µM]	MODE [µM]	D/214 [µM]	DIFF. STRESS [MPA]	LOG (D) [µM]	LOG (DIFF. STRESS) [MPA]	D/214 [µM]	DIFF. STRESS [MPA]	LOG (D) [µM]	LOG (DIFF. STRESS) [MPA]
452.62	ZW_MaP_16																						
959.20	ZW_MaP_13	499	14.69	840.97	116.36	149.33	125.82	50.00								0.70	1.37	2.17	0.14				
1518.00	ZW_MaP_20	493	8.29	1107.78	92.50	144.77	152.74	40.00								0.68	1.40	2.16	0.15				
1467.00	ZW_MaP_09	173	9.92	690.47	143.20	168.32	112.03	100.00								0.79	1.23	2.23	0.09				
1505.80	ZW_MaP_04_g																						
650.80	ZW_MaP_14	218	11.95	882.98	80.25	120.44	113.01	20.00								0.56	1.65	2.08	0.22				
591.90	ZW_MaP_15	472	8.92	1530.84	117.73	157.62	167.39	50.00								0.74	1.30	2.20	0.12				
991.00	ZW_MaP_21	137	7.81	535.13	63.17	107.34	105.51	30.00								0.50	1.82	2.03	0.26				
1444.50	ZW_MaP_10	328	12.48	949.76	112.11	156.42	141.52	40.00								0.73	1.31	2.19	0.12				
1028.00	ZW_MaP_12																						
1441.00	ZW_MaP_22	173	4.74	278.35	54.30	69.25	56.57	20.00								0.32	2.67	1.84	0.43				
268.18	ZW_MaP_28																						
1190.47	ZW_MaP_11	1284	9.18	1121.54	94.73	133.90	121.60	50.00	499	9.70	578.45	83.10	112.60	93.17	60.00	0.63	1.50	2.13	0.18	0.53	1.75	2.05	0.24
1503.26	ZW_MaP_07	287	12.84	934.47	97.11	145.00	135.04	40.00	124	21.47	934.47	149.38	206.06	170.45	50.00	0.68	1.40	2.16	0.15	0.96	1.03	2.31	0.01
605.00	ZW_MaP_23	15	36.06	253.55	99.08	108.94	68.30	100.00								0.51	1.80	2.04	0.25				
1006.30	ZW_MaP_24	223	5.51	427.78	55.72	78.85	73.68	20.00								0.37	2.38	1.90	0.38				
1461.00	ZW_MaP_25								504	28.67	892.73	185.87	222.91	144.86	130.00					1.04	0.97	2.35	-0.02
1294.71	ZW_MaP_26	173	5.77	376.01	40.93	60.94	54.36	30.00								0.28	2.98	1.78	0.47				
1604.00	ZW_MaP_27	344	5.83	624.77	61.53	94.25	96.41	10.00								0.44	2.04	1.97	0.31				

		ALL GRAINS							MEGA-GRAINS							DIFFERENTIAL STRESS ALL GRAINS				DIFFERENTIAL STRESS MEGA GRAINS			
DEPTH TOP	THIN SECTION	NUMBER OF GRAINS	MIN [µM]	MAX [µM]	MEDIAN [µM]	AVERAGE [µM]	STD_DEVIATION [µM]	MODE [µM]	NUMBER OF GRAINS	MIN [µM]	MAX [µM]	MEDIAN [µM]	AVERAGE [µM]	STD_DEVIATION [µM]	MODE [µM]	D/214 [µM]	DIFF. STRESS [MPA]	LOG (D) [µM]	LOG (DIFF. STRESS) [MPA]	D/214 [µM]	DIFF. STRESS [MPA]	LOG (D) [µM]	LOG (DIFF. STRESS) [MPA]
1393.68	ZW_MaP_29																						
1400.88	ZW_MaP_05_g																						
1469.27	ZW_MaP_08																						
267.39	ZW_MaP_30																						
542.23	ZW_MaP_02_g																						
1090.63	ZW_MaP_31																						
242.70	ZW_MaP_01_g																						
1003.13	ZW_MaP_32	465	13.40	1248.03	133.45	185.16	174.68	50.00								0.87	1.13	2.27	0.05				
1627.58	ZW_MaP_03_g																						
1795.01	ZW_MaP_06	4528	6.73	1098.04	76.77	107.37	96.69	30.00	3364	0.20	3936.67	77.94	145.02	267.50	30.00	0.50	1.82	2.03	0.26	0.68	1.40	2.16	0.15
421.95	ZW_MaP_33	515	11.39	868.37	81.33	114.96	105.23	60.00	91	14.71	868.37	136.27	188.38	175.36	30.00	0.54	1.72	2.06	0.23	0.88	1.12	2.28	0.05

Discussion

The Kristallbrockensalz is widespread within the Zechstein basin. It is generally interpreted to have formed out of a layer cake of fine-grained matrix salt, layers of single crystalline Halite, and thin Anhydrite layers (KEM-17 Barradeel). The Kristallbrocken are inferred to form out of this sediment by deformation, resulting in a kind of Augengneiss structure, with the Kristallbrocken decreasing in size with tectonic strain. Richter-Bernburg, (1953) described 'Trümmersalze' with 'Kristallbrocken' salt as large, sharp-edged crystal individuums inside a fine crystallized matrix. The structural characteristics of the 'Kristallbrockensalt' were studied and the observed microstructures of Kristallbrocken were attributed to brittle deformation and a strong competence contrast from porphyroclastic 'Kristallbrockensalt' to fine-grained, mylonitic matrix Halite (Küster et al., 2010, pg.98). The same studies also suggest that matrix Halite was secondary, replacing Kristallbrocken by recrystallization. The inferred strong rheology contrast was suggested to be related to 'monocrystallinity' (large grain size) and the abundant inclusions in Kristallbrocken by restricting dislocation mobility (Küster et al., 2008).

The overall microstructure of the samples shows a tectonically strongly deformed, recrystallized rock salt. Fluid-assisted dynamic grain boundary migration recrystallization, dislocation creep and pressure solution are interpreted to have been the main deformation mechanisms during the evolution of this salt body.

"*In most materials which deform by dislocation creep processes, the steady state subgrain size is inversely proportional to the stress difference (σ_1-σ_3) and independent of other variables.*

The relation is: $D=k\sigma^{-m}$

where D is the average subgrain size in µm, k and m are material constants and σ is the differential stress in MPa. Two recent datasets exist for experimentally deformed rock salt (Carter et al., 1993) where subgrain size and stress were measured. Plotting those data together, the parameters of the least squares fit line become k=215 and m=-1.15 (correlation coefficient=0.90)." (Schleder and Urai, 2005).

We used the correlation equation proposed by Schleder and Urai (2005), based i.a. on data from Carter et al., 1993 (Fig. 15a), to estimate the differential stress from subgrains measured in the reflected light micrographs. The results imply that the sampled sections of the Zuidwending salt dome underwent deformation at differential stresses between 1.2 and 1.8MPa (derived from average subgrain size from summarized measurements in matrix Halite grains and Halite mega-grains (Fig. 11c, Fig. 15b). In agreement with the subgrain size measurements by Barabasch et al., (2023, fig. 10) we find that subgrains in fine-grained matrix Halite are slightly smaller than subgrains in the associated mega-grains (Fig. 15). Considering the uncertainties in the calibrations and differences in measurement methods, we infer differential stress between 1 and 2.5 MPa, interpreted as the highest differential stress seen by the salt, during tectonic deformation. This differential stress is inferred to be much lower at present, due to relaxation in the tectonically quiet Tertiary.

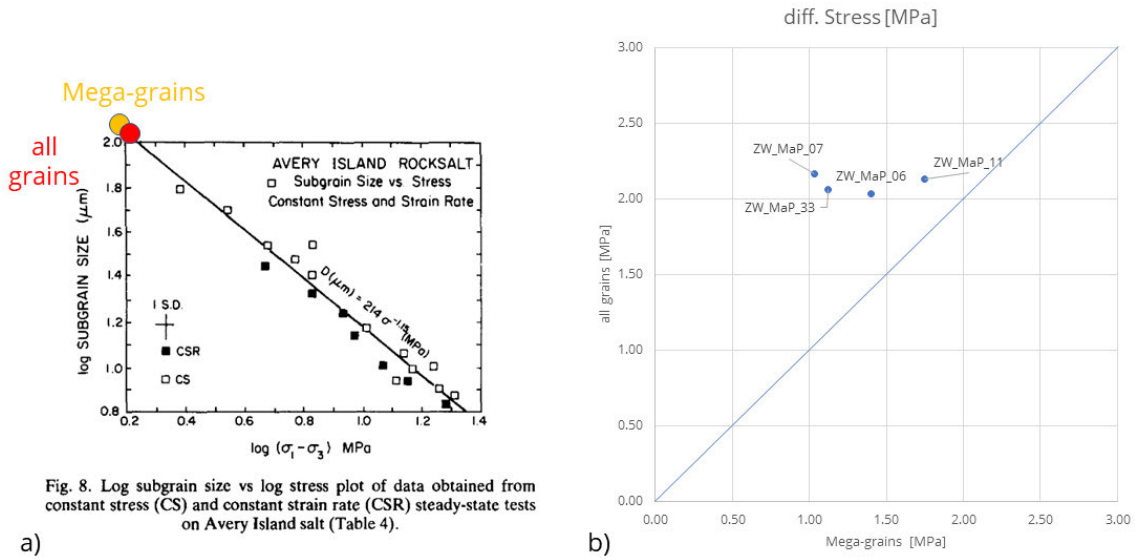

Fig. 8. Log subgrain size vs log stress plot of data obtained from constant stress (CS) and constant strain rate (CSR) steady-state tests on Avery Island salt (Table 4).

Fig. 15 a) Graph from Carter et al., 1993 with result of subgrain size piezometry for the mega-grains (yellow dot), the matrix Halite grains (red dot) and the average of all subgrains (blue dot); b) Graph showing derived differential stress from all grains vs. derived differential stress from matrix grains.

The presence of subgrains (e.g., Fig. 16) shows that the Halite mega-grains deformed by dislocation creep, and were bent and boudinaged by deformation, in agreement with earlier publications. They are slowly replaced by fine-grained Halite by fluid assisted grain boundary migration recrystallization (e.g., Fig. 1 and Fig. 16).

In contrast, recrystallized Halite matrix is inferred to deform by a combination of dislocation creep, visible in occasionally preserved subgrains and slip bands and pressure solution accompanied by dynamic recrystallization (Fig. 17a-d). The presence of folded and boudinaged Anhydrite layers (e.g., Fig. 1a and Fig. 17e) shows that the fine-grained Halite matrix deformed to much higher strains than the mega-grains. Overall, the samples examined were similar on the cm to nm scale with respect to the microstructural features described above. The samples also showed no significant differences when distinguishing between litho-classes E, F, G and H, except that the thin, fine-grained Anhydrite layers seemed to protect the adjacent mega-grains from the recrystallisation front (e.g., Fig. 1b).

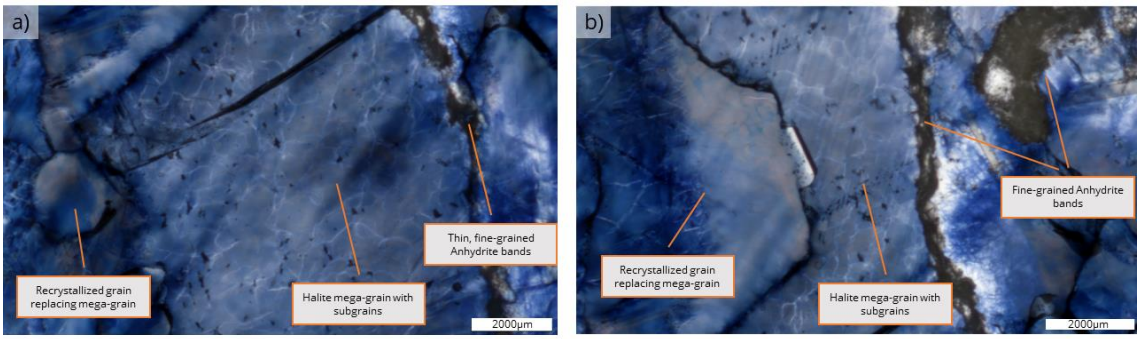

Fig. 16 Transmitted light micrographs of the mega-grains in Gamma-irradiated Kristallbrockensalz. The mega-grains are full of subgrains indicating dislocation creep. Sample ID is: ZW_MaP_05_g (ZWD-A7B 1_13_1400.88).

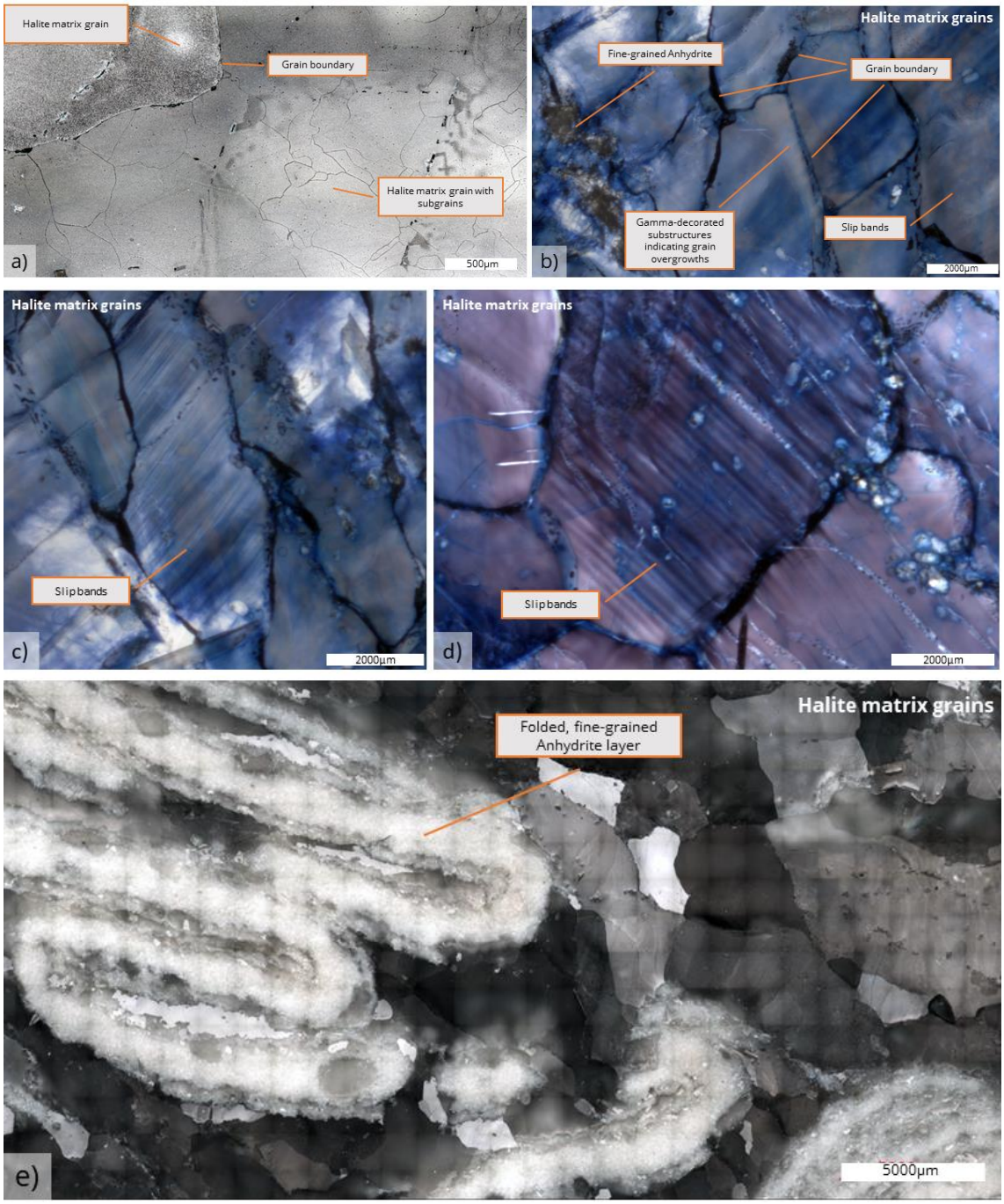

Fig. 17 a) Reflected-light micrograph showing subgrains within mega-grain, b) Transmitted light micrograph showing matrix grains. The microstructure shows fluid-assisted grain boundary migration recrystallization. c) and d) Slip bands in elongated matrix Halite grains indicate deformation by dislocation creep and pressure solution. e) The fine-grained matrix underwent much higher strains than in the mega-grains as shown by the ruptured and folded Anhydrite layers.

To a first approximation, the matrix fine-grained rock salt's rheology can be described by a two-mechanism creep law which as a first approximation can be inferred based on the measured grainsize with a power law part and a change to Newtonian, pressure solution dominated creep at low differential stress. On the other hand, the mega-grains deform only by dislocation creep. Fig. 18 shows that at low differential stress relevant to cavern operation, the matrix and mega-grains creep at strain rates, which are three orders of magnitude different, as also described in the study by Barabasch et al., (2023, fig. 9).

The rheology of the investigated parts of the Zuidwending salt dome during its evolution is thus inferred to be a mixture rheology, complex and nonlinear strongly dependent on the fraction of mega-grains, with a local variance in strain rate of several orders of magnitude at the same differential stress between the mega-grains and the fine-grained matrix, caused by the difference in (grain-size dependent) deformation mechanisms, and the variable fraction of mega-grains Fig. 19.

Based on our results we fully support the recommendation by Barabasch et al., (2013) which is cited below:

"In current constitutive models of salt engineering (Albrecht et al., 1993; Hunsche et al., 2003; Bräuer et al., 2011; Kukla et al., 2011; Liu, W. et al., 2017; Popp, 2022) it was long recognized that the creep strain rate of rock salt (as measured at relatively high differential stress) can show several orders of magnitude differences, at the same differential stress and temperature. Based on an extensive dataset, such observations provided the basis for the definition of Kriechklassen which were used to model the evolution of engineered structures (Liu, W. et al., 2017) and are still used to describe a non-Newtonian rheology in salt tectonics numerical modeling (Granado et al., 2021). However, as has been reviewed above, extrapolation of these data to low differential stress predicts orders of magnitude lower creep rates than measured in experiments (Brouard and Bérest, 1998; Bérest et al., 2019) and predicted by microphysical models of pressure solution creep (Spiers et al., 1986; Urai et al., 1986b; Spiers et al., 1990). Integration of these mechanisms into engineering constitutive equations is sometimes conducted (e.g. Zill et al., 2022; Buijze et al., 2022). However, it requires data on the grain size of the rock salt to be modeled, together with microstructural characterization, and we recommend to include grain sizes in engineering prediction and create pressure solution-creep classes."

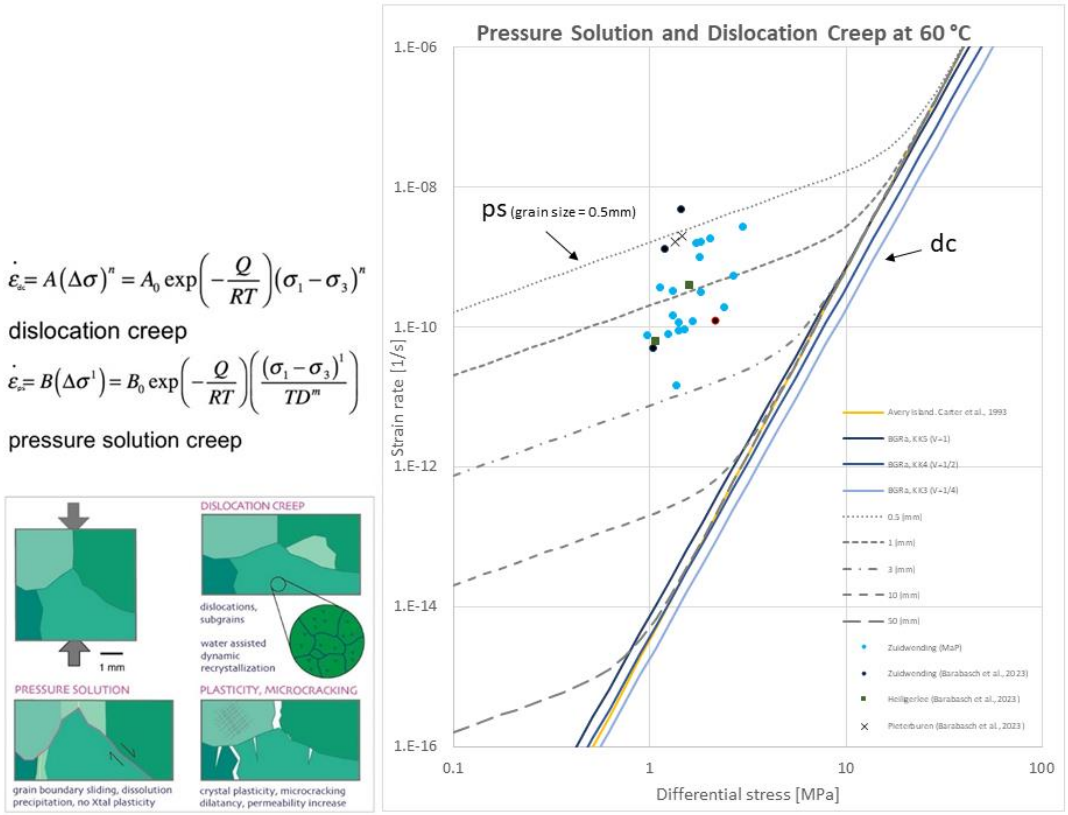

Fig. 18 Prediction of long-term creep rheology of Zuidwending rock salt. Halite mega-grains deform by dislocation creep (average diff. stress is 2MPa, not covered by the diagram y-axis). Recrystallized Halite deforms by dislocation creep and pressure solution (data series Zuidwending (MaP)). The two grainsizes have a large contrast in rheology at 1MPa differential stress. Rheology of the salt is determined by the properties of the mixture.

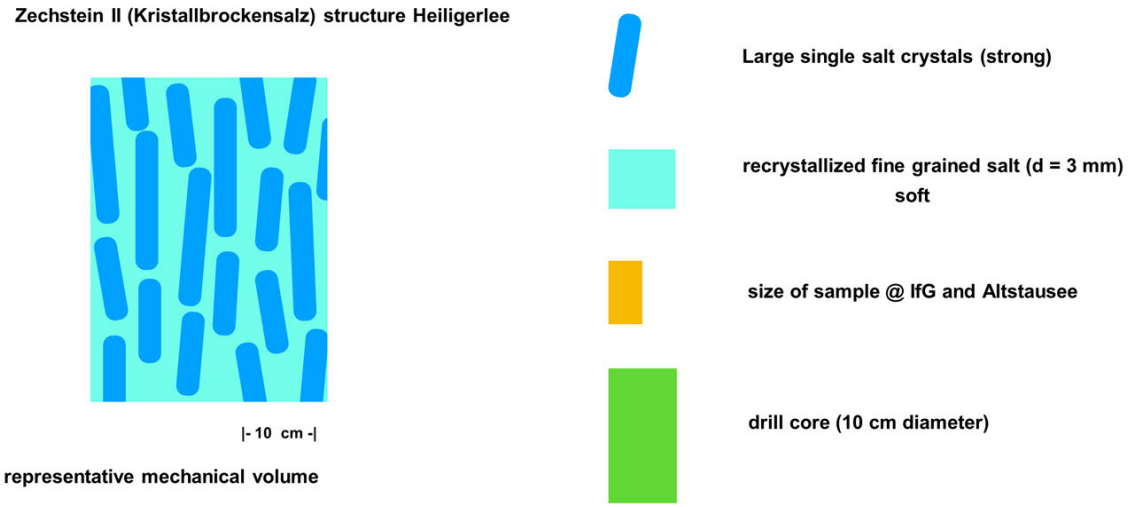

Fig. 19 Sketch illustrating the Zechstein II (Kristallbrockensalz) structure at meter-scale. The fine-grained salt is weak and mega-grains strong at low differential stress. The key for determining the rheology is the fraction and distribution of mega-grains. The rheology is anisotropic and nonlinear.

Summarizing remarks

We investigated the microstructure of 30 core pieces selected in ZW1.1 in terms of microtectonic evolution and quantified the corresponding parameters to be used to constrain the microstructural and rheological properties to eventually derive a constitutive law for salt in the vicinity of a cavern (ZW4.1), together with information from other work packages. The performed work, the results as well as the interrelation to the, mainly successive, work packages is illustrated in Table 6, in addition to the illustration of the interdependencies of the different work packages given in the CCC proposal [1](Figure 2. Project organization Zuidwending).

The role of grain size, subgrain size, dislocations, grain boundary structure, impurity content and distribution, solid solution content in the development of microstructure and the related mechanical properties of the salt is described in great detail in the KEM-17 report (Over-pressured salt solution mining caverns and leakage mechanisms, Phase 1: micro-scale processes) and references therein. The reader is referred to pp. 9-20 (Rheology and Microphysical deformation mechanisms of salt rocks).

Table 6 Overview results, interpretation, and interrelation to other work packages.

Task ZW1.2	***Result ZW1.2***	***linked work packages***
Microtectonic observations/interpretation (texture, grain boundary structure, microstructural processes, rheology)	***Texture:*** *fine-grained, recrystallized matrix Halite with slightly elongated grains, deformed mega-grains; thin, deformed Anhydrite layers.* ***Grain boundary structure****: overall tight grain boundaries with equilibrated fluid inclusion arrays, some dilatant.* ***Microstructural processes:*** *mega-grains deformed by brittle deformation (boudinage) and dislocation creep; matrix Halite deformed by combined dislocation creep, pressure solution creep, and dynamic recrystallization.* ***Rheology:*** *mixed and non-linear, strain rate strongly dependent on local presence of mega-grains.*	*Input work package:* ***ZW1.1*** *Selection of representative or typical core pieces for microscale analyses, integrated with deformation and permeation experiments* *Direct output in work packages:* ***ZW1.4****: Geological and geophysical constraints for the evolution and today's state of the salt dome* ***ZW2.1****: Microscale analysis of selected deformed material* ***ZW2.2****: Design, supervision and analysis of deformation experiments at IFG* ***ZW2.3****: Determine pressure-solution creep parameters in the far field for deviatoric stresses less than 2 MPa* ***ZW2.4****: Determine feasible limits of stress and strain rates in the low stress/low strain rate regime* ***ZW2.6****: Determine a site-specific constitutive model that is adapted to the local requirements*
Grain size measurement	*Average median grain size: 1.2 mm (Std.Dev 2.9 mm)*	
Derive max. differential stress from subgrain size	*Average derived differential stress: 2MPa (average min: 1.8 MPa, average max: 2.3 MPa)*	
Assess second phase content	*Bulk second phase content litho-class F: 5.0 Vol.%, litho-class G: 5.8 Vol.%,litho-class H: 17.7 Vol.%,*	

[1] JOINT PROJECT PROPOSAL: Abandonment of solution mining cavern field Zuidwending, 15 Sepetember 2021, by CCC Cavern Closure Consortium

Task ZW1.2	*Result ZW1.2*	*linked work packages*
		***ZW3.1**: Microscale analysis of selected permeated material* ***ZW3.2**: Design, supervision and interpretation of permeation experiments* ***ZW4.1**: Model for constitutive law in salt surrounding the cavern*

Literature

Albrecht, H., Hunsche, U., and Schulze, O., 1993. Results from the application of the laboratory test program for mapping homogeneous parts in the Gorleben salt dome, 10th national rock mechanics symposium in Aachen, November 1992; Geotechnik-Sonderheft 1993, 155–158, Glückauf, Essen.

Barabasch, J., Schmatz, J., Klaver, J., Schwedt, A., Urai, J.L., 2023. Large grain-size-dependent rheology contrasts of Halite at low differential stress: evidence from microstructural study of naturally deformed gneissic Zechstein 2 rock salt (Kristallbrockensalz) from the northern Netherlands. Solid Earth, 14, 271–291, https://doi.org/10.5194/se-14-271-2023.

Bérest, P., Gharbi, H., Brouard, B., Brückner, D., DeVries, K., Hévin, G., Hofer, G., Spiers, C., and Urai, J. L., 2019. Very Slow Creep Tests on Salt Samples, Rock. Mech. Rock. Eng., 52, 2917–2934, https://doi.org/10.1007/s00603-019-01778-9.

Bräuer, V., Eickenmeier, R., Eisenburger, D., Grissemann, C., Hesser, J., Heusermann, S., Kaiser, D., Nipp, H.-K., Nowak, T., Plischke, I., Schnier, H., Schulze, O., Sönnke, J., and Weber, J. R, 2011. Description of the Gorleben site part 4: Geotechnical exploration of the Gorleben salt dome, Bundesanstalt für Geowissenschaften und Rohstoffe (BGR), Hannover, Germany, ISBN 978-3-9814108-0-8.

Brouard, B. and Bérest, P., 1998. A tentative classification of salts according to their creep properties, SMRI Spring 1998 Meeting, 19–22 April 1998, New Orleans, Louisiana, USA, 18–38.

Hunsche, U. and Hampel, A., 1999. Rock salt – the mechanical properties of the host rock material for a radioactive waste repository, Eng. Geol., 52, 271–291, https://doi.org/10.1016/S0013-7952(99)00011-3.

KEM-17 https://www.sodm.nl/binaries/staatstoezicht-op-de-mijnen/documenten/rapporten/2020/02/11/onderzoek-langetermijnrisicos-afsluiten-zotcavernes/KEM-17+Micro-scale.pdf

Küster, Y., Leiss, B., Schramm, M., 2010. Structural characteristics of the Halite fabric type 'Kristallbrocken' from the Zechstein Basin with regard to its development. International Journal of Earth Sciences 99, 505–526. https://doi.org/10.1007/s00531-008-0399-8

Kukla, P. A., Pechnig, R., and Urai, J. L., 2011. Sichtung und Bewertung der Standortdaten Gorleben: Bericht zum Arbeitspaket 2: Vorläufige Sicherheitsanalyse für den Standort Gorleben, Gesellschaft für Anlagen- und Reaktorsicherheit (GRS) mbH, Cologne, Germany, ISBN 978-3-939355-52-6.

Liu, W., Völkner, E., Minkley, W., and Popp, T., 2017. Zusammenstellung der Materialparameter für THM-Modellberechnungen: Ergebnisse aus dem Vorhaben KOSINA, report, Bundesanstalt für Geowissenschaften und Rohstoffe (BGR), Hannover, Germany.

Popp, T.: Eigenschaften und Potential stratiformer Salz-Formationen für die Endlagerung hochradioaktiver Abfälle, report, Institut für Gebirgsmechanik IfG, Leipzig, Germany, 2022.

Richter-Bernburg, G., 1953. Über salinare Sedimentation. Zeitschrift der Deutschen Geologischen Gesellschaft 105, 593–645.

Spiers, C. J., Urai, J. L., Lister, G. S., Boland, J. N., and Zwart, H. J., 1986. The influence of fluid-rock interaction on the rheology of salt rock, Commission of the European Communities, Luxembourg, EUR 10399 EN, ISBN 92-825-6214-X.

THIEMEYER, N., ZULAUF, G., MERTINEIT, M., LINCKENS, J., PUSCH, M. & HAMMER, J. 2016. Microfabrics and 3D grain shape of Gorleben rock salt: Constraints on deformation mechanisms and palaeodifferential stress. Tectonophysics 676, 1-19.

Urai, J. L., Means, W. D., and Lister, G. S., 1986a. Dynamic Recrystallization of Minerals, in: Mineral and Rock Deformation, American Geophysical Union (AGU), 161–199, https://doi.org/10.1029/GM036p0161.

Urai, J. L., Spiers, C. J., Zwart, H. J., and Lister, G. S., 1986b. Weakening of rock salt by water during long-term creep, Nature, 324, 554–557, https://doi.org/10.1038/324554a0.

Appendix A

Catalogue with sample selection, further micrographs with interpretation, and grain/subgrain segmentation details; grain size distribution, subgrain size distribution for the individual samples.